

RESEARCH ARTICLE

Practical computation of the diffusion MRI signal based on Laplace eigenfunctions: permeable interfaces

Syver Døving Agdestein¹ | Try Nguyen Tran² | Jing-Rebecca Li^{*3}

¹Centre de Mathématiques Appliquées,
Ecole Polytechnique, Route de Saclay,
91128 Palaiseau Cedex, France

²Ho Chi Minh City, Vietnam

³INRIA Saclay - Equipe DEFI, CMAP,
Ecole Polytechnique, Route de Saclay,
91128 Palaiseau Cedex, France

Correspondence

*Corresponding author. Email:
jingrebecca.li@inria.fr

Abstract

The complex transverse water proton magnetization subject to diffusion-encoding magnetic field gradient pulses in a heterogeneous medium such as brain tissue can be modeled by the Bloch-Torrey partial differential equation. The spatial integral of the solution of this equation in realistic geometry provides a gold-standard reference model for the diffusion MRI signal arising from different tissue micro-structures of interest.

A closed form representation of this reference diffusion MRI signal has been derived twenty years ago, called Matrix Formalism, that makes explicit the link between the Laplace eigenvalues and eigenfunctions of the tissue geometry and its diffusion MRI signal. In addition, once the Laplace eigendecomposition has been computed and saved, the diffusion MRI signal can be calculated for arbitrary diffusion-encoding sequences and b-values at negligible additional cost.

In a previous publication, we presented a simulation framework that we implemented inside the MATLAB-based diffusion MRI simulator SpinDoctor that efficiently computes the Matrix Formalism representation for biological cells subject to impermeable membrane boundary conditions. In this work, we extend our simulation framework to include geometries that contain permeable cell membranes. We describe the new computational techniques that allowed this generalization and we analyse the effects of the magnitude of the permeability coefficient on the eigen-decomposition of the diffusion and Bloch-Torrey operators.

This work is another step in bringing advanced mathematical tools and numerical method development to the simulation and modeling of diffusion MRI.

KEYWORDS:

Bloch-Torrey equation, diffusion MRI, finite elements, simulation, Matrix Formalism, Laplace eigenfunctions, permeability.

1 | INTRODUCTION

Diffusion MRI is an imaging modality that can be used to probe the tissue micro-structure by encoding the incoherent motion of water molecules with magnetic field gradient pulses. Incoherent motion during the diffusion-encoding time causes a signal attenuation from which the apparent diffusion coefficient (ADC), and possibly higher order diffusion terms, can be calculated^{1,2,3}. For free diffusion, the root of the mean squared displacement of molecules is given by $\bar{x} = \sqrt{2dDt}$, where d is the spatial dimension, D is the intrinsic diffusion coefficient, and t is the diffusion time. In biological tissue, diffusion is usually hindered or restricted (for example, by cell membranes) and the mean square displacement is smaller than in the case of free diffusion. This deviation from free diffusion can be used to infer information about the tissue micro-structure.

Using diffusion MRI to get tissue structural information in the brain has been the focus of much experimental and modeling work in recent years^{4,5,6,7,8,9,10,11,12,13,14,15,16,17,18,19}. In terms of modeling, the predominant approach up to now has been adding the contributions to the diffusion MRI signal from simple geometrical components and extracting model parameters of interest. Numerous biophysical models subdivide the tissue into compartments described by spheres, ellipsoids, cylinders, and the extra-cellular space^{12,13,14,16,20,21,22,17,23,24}. Some model parameters of interest include axon diameter and orientation, neurite density, dendrite structure, the volume fraction and size distribution of cylinder and sphere components and the effective diffusion coefficient or tensor of the extra-cellular space. The need for a mathematically rigorous model of the diffusion MRI signal arising from realistic cellular structures was re-iterated in recent review papers^{25,26,27}.

There is a gold-standard reference model of the diffusion MRI signal, it is the Bloch-Torrey partial differential equation (PDE) that describes the time evolution of the complex transverse water proton magnetization subject to diffusion-encoding magnetic field gradient pulses. For this model to be the gold-standard, it should be posed in realistic tissue and cell geometries, typically, heterogeneous media containing different cell structures and the extra-cellular space. The spatial integral of the solution of the PDE provides a reference model for the diffusion MRI signal arising from the geometry of interest. Because of the high computational cost of solving the Bloch-Torrey equation in complicated cell geometries, this gold standard model has been used primarily as a “forward model” or “simulation framework”, in which one changes the inputs parameters such as cell geometry, intrinsic diffusion coefficient, membrane permeability, and study the resulting changes to the MRI signal. This is in contrast to “inverse models”, which are used to estimate the model parameters of interest from the MRI signal, the idea being that the “inverse models” have been formulated in such a way so that the model parameters can be correlated to biological information in the imaging voxel. “Inverse models” include the biophysical models cited above. Nevertheless, given the recent availability of vastly powerful computational resources and computer memory, it is possible that simulation frameworks may become directly useful for parameter estimation in the future (for some recent works in this direction, see^{18,28}).

In²⁹, we presented SpinDoctor, a MATLAB-based diffusion MRI simulation toolbox that solves the Bloch-Torrey PDE using the Finite Element Method (FEM) and an adaptive time stepping method. SpinDoctor provides a user-friendly interface to easily define cell configurations relevant to the brain white matter. In³⁰, we presented a module of SpinDoctor called the Neuron Module that enables diffusion MRI simulations for a group of pyramidal neurons and a group of spindle neurons whose morphological descriptions were found in the neuron repository *NeuroMorpho.Org*³¹. The key to making accurate simulation possible is the use of high quality finite element meshes for the neurons. We refer the reader to^{29,30} for implementation details and timing comparisons with Monte-Carlo (random walk) type simulations.

Taking the Bloch-Torrey equation as the gold-standard reference model, a closed form representation of the reference signal has been derived twenty years ago, that is based on the eigenvalues and eigenfunctions of the Laplace operator in the relevant cell geometry. This representation frequently goes under the name of Matrix Formalism. The version that uses the impulse approximation of the diffusion-encoding sequence is first found in³² and the version that uses the piecewise constant approximation of the diffusion-encoding sequence is first found in³³. There have been numerous works using Matrix Formalism in elementary geometries such as the line segment, the disk, and the sphere, as well as geometries which can be written as tensor products of these elementary geometries. We cite^{34,35,36} and refer the reader to the literature surveys on the Matrix Formalism contained in those articles.

There are two advantages to the Matrix Formalism signal representation. First, the analytical advantage is that this representation makes explicit the link between the Laplace eigenvalues and eigenfunctions of the biological cell and its diffusion MRI signal. This clear link may help in the formulation of reduced models of the diffusion MRI signal that is closer to the physics of the problem. Second, the computational advantage is that once the Laplace eigendecomposition has been computed and saved, the diffusion MRI signal can be calculated for arbitrary diffusion-encoding sequences and b-values at negligible additional cost. This will make it possible to use the Matrix Formalism as the inner loop of optimization procedures.

⁰**Abbreviations:** ADC, Apparent Diffusion Coefficient; BT, Bloch-Torrey; ECS, Extra-Cellular Space; FEM, Finite Element Method; FPK, Finite Pulse Karger model; HADC, Homogenized Apparent Diffusion Coefficient MF, Matrix Formalism; MRI, Magnetic Resonance Imaging; ODE, Ordinary Differential Equation; OGSE, Oscillating Gradient Spin Echo; PDE, Partial Differential Equation; PGSE, Pulsed-Gradient Spin Echo

Until recently, Matrix Formalism, as a closed form signal representation, though mathematically elegant, has not been used as a practical way of computing the diffusion MRI signal in complicated geometries. The calculation of the Laplace eigendecomposition in complicated geometries using Monte-Carlo based simulations would be essentially impossible due to computational time and memory limitations. In a recent work³⁷, using the FEM, we implemented inside SpinDoctor the computation of the Matrix Formalism representation for biological cells subject to *impermeable* boundary conditions and showed its usefulness in understanding the diffusion MRI signal from realistic neuron geometries. In this work, we extend our simulation framework to include geometries that contain *permeable* cell membranes. The Matrix Formalism has been previously applied with permeable membranes for simple geometries like multilayered plates, spheres or cylinders^{34,38}, with up to thousands of permeable cell membranes in the 1D-case³⁹. The formulation we propose is valid for arbitrary multi-compartment geometries with three-dimensional shapes. A major advantage of this work is that once the eigenfunctions have been computed, many diffusion-encoding sequences, b-values, and diffusion directions can be simulated at negligible additional cost.

2 | THEORY

The geometrical configuration that we consider in this paper is a connected three-dimensional domain $\Omega = \bigcup_{i=1}^{N_{\text{cmt}}} \Omega_i \subset \mathbb{R}^3$ consisting of N_{cmt} compartments $\{\Omega_i\}_{1 \leq i \leq N_{\text{cmt}}}$. The permeable interface between two compartments is denoted by $\Gamma_{ij} = \Omega_i \cap \Omega_j$ for $i \neq j, (i, j) \in \{1, \dots, N_{\text{cmt}}\}^2$. For $i = j$, we let $\Gamma_{ii} = \emptyset$ for the ease of notation. Finally, let $\partial\Omega$ denote the outer boundary of the domain, and $\Gamma_i = \Omega_i \cap \partial\Omega$ its restriction to Ω_i . Note that for compartments that do not touch, we have $\Gamma_{ij} = \emptyset$. Similarly, we have $\Gamma_i = \emptyset$ for compartments that do not touch the outer boundary.

If the geometry consists of N_{cell} cells enclosed in an extra-cellular space (ECS), the ECS will be the last compartment. For spherical cells, only the ECS has an outer boundary, and all cells have an interface with the ECS. The cells may also contain nuclei. For cylindrical cells, the top and bottom of each cylinder is an outer boundary. The cells may have myelin layers.

2.1 | Bloch-Torrey PDE

In diffusion MRI, a time-varying magnetic field gradient is applied to the tissue to encode water diffusion. Denoting the effective time profile of the diffusion-encoding magnetic field gradient by f , and letting the vector $\mathbf{g} \in \mathbb{R}^3$ contain the amplitude and direction information of the magnetic field gradient, the complex transverse water proton magnetization in the rotating frame satisfies the Bloch-Torrey PDE (BTPDE):

$$\frac{\partial}{\partial t} M_i(\mathbf{x}, t) = -i\gamma f(t) \mathbf{g} \cdot \mathbf{x} M_i(\mathbf{x}, t) + \nabla \cdot D_i \nabla M_i(\mathbf{x}, t), \quad \mathbf{x} \in \Omega_i, \quad i \in \{1, \dots, N_{\text{cmt}}\}, \quad (1)$$

where $\gamma = 2.67513 \times 10^8 \text{ rad s}^{-1} \text{ T}^{-1}$ is the gyromagnetic ratio of the water proton, i is the imaginary unit, and D_i is the intrinsic diffusion coefficient in the compartment Ω_i . The magnetization is a function of position \mathbf{x} and time t , and depends on the diffusion gradient vector \mathbf{g} and the time profile f . We denote the restriction of the magnetization in Ω_i by M_i . Note that the magnetization may be discontinuous at the interfaces Γ_{ij} . In the following, inside volume integrals, we will denote by $M(\mathbf{x}, t)$ the global magnetization for $\mathbf{x} \in \Omega$, uniquely defined almost everywhere.

The initial conditions are assumed to be compartment-wise constant:

$$M_i(\mathbf{x}, 0) = \rho_i, \quad \mathbf{x} \in \Omega_i, \quad i \in \{1, \dots, N_{\text{cmt}}\}, \quad (2)$$

where ρ_i is the initial spin density in compartment Ω_i .

The outer boundary conditions for the BTPDE are given by

$$D_i \nabla M_i(\mathbf{x}, t) \cdot \mathbf{n}_i(\mathbf{x}) = 0, \quad \mathbf{x} \in \Gamma_i, \quad i \in \{1, \dots, N_{\text{cmt}}\}, \quad (3)$$

where \mathbf{n}_i is the unit outward pointing normal vector of compartment Ω_i . This conserves the total number of spins in the domain. Note that we may have $\Gamma_i = \emptyset$, as all the compartments do not necessarily touch the outer boundary.

The BTPDE also needs to be supplemented by interface conditions. We recall that the interface between Ω_i and Ω_j is Γ_{ij} . The two interface conditions on Γ_{ij} are the flux continuity and a condition that incorporates a permeability coefficient $\kappa_{ij} \geq 0$ across Γ_{ij} :

$$D_i \nabla M_i(\mathbf{x}, t) \cdot \mathbf{n}_i(\mathbf{x}) = -D_j \nabla M_j(\mathbf{x}, t) \cdot \mathbf{n}_j(\mathbf{x}), \quad \mathbf{x} \in \Gamma_{ij}, \quad (i, j) \in \{1, \dots, N_{\text{cmt}}\}^2, \quad (4)$$

$$D_i \nabla M_i(\mathbf{x}, t) \cdot \mathbf{n}_i(\mathbf{x}) = \kappa_{ij} (c_{ij} M_j(\mathbf{x}, t) - c_{ji} M_i(\mathbf{x}, t)), \quad \mathbf{x} \in \Gamma_{ij}, \quad (i, j) \in \{1, \dots, N_{\text{cmt}}\}^2. \quad (5)$$

Here, the permeability coefficient characterizes the membrane only ($\kappa_{ij} = \kappa_{ji}$), and is assumed to be non-negative. If $\kappa_{ij} = 0$, the interface Γ_{ij} behaves like an infinitely thin hard wall, similar to the outer boundary in Eq. (3).

The two weights c_{ij} and c_{ji} account for the spin density equilibrium between the two compartments. These may both be set to 1, in which case a uniform spin density across compartments is favored in the absence of a gradient. For different initial spin densities $\rho_i \neq \rho_j$, we also allow for non-symmetrical weights, for example $c_{ij} = \frac{2\rho_i}{\rho_i + \rho_j}$ and $c_{ji} = \frac{2\rho_j}{\rho_i + \rho_j}$ as proposed in⁴⁰. This ensures that the non-uniform initial spin density is preserved if the gradient \mathbf{g} is zero. The normalization coefficient $2/(\rho_i + \rho_j)$ ensures that $c_{ij} = c_{ji} = 1$ if $\rho_i = \rho_j$.

Some commonly used time profiles (diffusion-encoding sequences) are the pulsed-gradient spin echo (PGSE) sequence² and the oscillating gradient spin echo (OGSE) sequence^{41,42}. Here, we will consider the PGSE sequence, with two rectangular pulses of duration δ , separated by a time interval $\Delta - \delta$, for which the profile f is

$$f(t) = \begin{cases} 1, & t_1 \leq t \leq t_1 + \delta, \\ -1, & t_1 + \Delta < t \leq t_1 + \Delta + \delta, \\ 0, & \text{otherwise,} \end{cases} \quad (6)$$

where t_1 is the starting time of the first gradient pulse, and T_e is the echo time at which the signal is measured (with $t_1 + \Delta \geq T_e/2$). In the following, we will set $t_1 = 0$ and $T_e = \Delta + \delta$ for simplicity.

The diffusion MRI signal is measured at echo time $t = T_e$. This signal is the spatial integral the final magnetization $M(\cdot, T_e)$:

$$S = \int_{\mathbf{x} \in \Omega} M(\mathbf{x}, T_e) d\Omega(\mathbf{x}), \quad (7)$$

In a diffusion MRI experiment, the pulse sequence (time profile f) is usually fixed, while \mathbf{g} is varied in amplitude (and possibly also in direction). The signal S is usually plotted against a quantity called the b -value. The b -value depends on \mathbf{g} and f and is defined as

$$b(\mathbf{g}, f) = \gamma^2 \|\mathbf{g}\|^2 \int_0^{T_e} \left(\int_0^s f(t) dt \right)^2 ds. \quad (8)$$

For PGSE, the b -value is²:

$$b(\mathbf{g}, \delta, \Delta) = \gamma^2 \|\mathbf{g}\|^2 \delta^2 (\Delta - \delta/3). \quad (9)$$

The reason for these definitions is that in a homogeneous medium, the signal attenuation is e^{-D^b} , where D is the intrinsic diffusion coefficient.

2.2 | Matrix Formalism signal representation

Using the Matrix Formalism^{32,33}, the diffusion MRI signal has the following representation for the PGSE sequence. Let $\{(\phi, \lambda)\}$ be the L^2 -normalized eigenfunctions and eigenvalues associated to the generalized Laplace operator¹ on the connected domain $\Omega = \bigcup_{i=1}^{N_{\text{cmt}}} \Omega_i$ satisfying

$$-\nabla \cdot D_i \nabla \phi^i(\mathbf{x}) = \lambda \phi^i(\mathbf{x}), \quad \mathbf{x} \in \Omega_i, \quad i \in \{1, \dots, N_{\text{cmt}}\}, \quad (10)$$

where $\phi^i(\mathbf{x})$ denotes the restriction of $\phi(\mathbf{x})$ to compartment Ω_i . The same boundary and interface conditions as for the BTPDE apply:

$$D_i \nabla \phi^i(\mathbf{x}) \cdot \mathbf{n}_i(\mathbf{x}) = -D_j \nabla \phi^j(\mathbf{x}) \cdot \mathbf{n}_j(\mathbf{x}), \quad \mathbf{x} \in \Gamma_{ij}, \quad (i, j) \in \{1, \dots, N_{\text{cmt}}\}^2, \quad (11)$$

$$D_i \nabla \phi^i(\mathbf{x}) \cdot \mathbf{n}_i(\mathbf{x}) = \kappa_{ij} (c_{ij} \phi^j(\mathbf{x}) - c_{ji} \phi^i(\mathbf{x})), \quad \mathbf{x} \in \Gamma_{ij}, \quad (i, j) \in \{1, \dots, N_{\text{cmt}}\}^2, \quad (12)$$

$$D_i \nabla \phi^i(\mathbf{x}) \cdot \mathbf{n}_i(\mathbf{x}) = 0, \quad \mathbf{x} \in \Gamma_i, \quad i \in \{1, \dots, N_{\text{cmt}}\}. \quad (13)$$

Let the solutions (ϕ, λ) to the above equations, (10-13), be denoted by $\{(\phi_n, \lambda_n)\}_{n \in \mathbb{N}^*}$. We assume the non-negative real-valued eigenvalues are ordered in non-decreasing order:

$$0 = \lambda_1 \leq \lambda_2 \leq \lambda_3 \leq \dots$$

If the domain Ω consists of only one contiguous group of compartments connected through a chain of permeable membranes, only the first eigenvalue will be zero, and the corresponding eigenfunction will be the only constant function. If there are $N_{\text{group}} \geq 2$ groups of connected

¹Here, the operator $\nabla \cdot D \nabla$ with the described permeable interface conditions will be referred to as a generalized Laplace operator, as opposed to the pure Laplace operator $\nabla \cdot \nabla$.

compartments completely separated by interior hard wall membranes, the first N_{group} eigenvalues will be zero:

$$0 = \lambda_1 = \dots = \lambda_{N_{\text{group}}} < \lambda_{N_{\text{group}}+1} \leq \dots,$$

and there will be N_{group} corresponding groupwise constant eigenfunctions. In the latter case, the equations may be rewritten separately for each connected subdomain to obtain a set of eigenvalues with a multiplicity of one, but the formulation is also valid in the global form with multiple zero eigenvalues. These two formulations will lead to an identical eigenfunction basis (up to a linear combination for the eigenvalues with multiplicity higher than one), where the basis of each subdomain is a subset of the global eigenfunction basis.

Let \mathbf{L} be the diagonal matrix containing the first N_{eig} Laplace eigenvalues:

$$\mathbf{L} = \text{diag}(\lambda_1, \lambda_2, \dots, \lambda_{N_{\text{eig}}}) \in \mathbb{R}^{N_{\text{eig}} \times N_{\text{eig}}}. \quad (14)$$

Let $\mathbf{A}(\mathbf{g})$ be the $N_{\text{eig}} \times N_{\text{eig}}$ matrix defined by:

$$\mathbf{A}(\mathbf{g}) = g_x \mathbf{A}^x + g_y \mathbf{A}^y + g_z \mathbf{A}^z, \quad (15)$$

where $\mathbf{g} = (g_x, g_y, g_z)^\top$ is the gradient vector and \mathbf{A}^x , \mathbf{A}^y , and \mathbf{A}^z are three symmetric $N_{\text{eig}} \times N_{\text{eig}}$ matrices whose entries are the first order moments in the coordinate directions of the product of pairs of eigenfunctions:

$$A_{mn}^x = \int_{\Omega} x \phi_m(\mathbf{x}) \phi_n(\mathbf{x}) d\Omega(\mathbf{x}), \quad (m, n) \in \{1, \dots, N_{\text{eig}}\}^2, \quad (16)$$

$$A_{mn}^y = \int_{\Omega} y \phi_m(\mathbf{x}) \phi_n(\mathbf{x}) d\Omega(\mathbf{x}), \quad (m, n) \in \{1, \dots, N_{\text{eig}}\}^2, \quad (17)$$

$$A_{mn}^z = \int_{\Omega} z \phi_m(\mathbf{x}) \phi_n(\mathbf{x}) d\Omega(\mathbf{x}), \quad (m, n) \in \{1, \dots, N_{\text{eig}}\}^2. \quad (18)$$

Then the Bloch-Torrey operator

$$-\nabla \cdot D\nabla + i\gamma \mathbf{g} \cdot \mathbf{x}$$

in the Laplace eigenfunction basis is given by the complex-valued matrix $\mathbf{K}(\mathbf{g})$:

$$\mathbf{K}(\mathbf{g}) = \mathbf{L} + i\gamma \mathbf{A}(\mathbf{g}). \quad (19)$$

The following matrix

$$\mathbf{H}(\mathbf{g}, f) = e^{-\delta \mathbf{K}^*} e^{-(\Delta - \delta) \mathbf{L}} e^{-\delta \mathbf{K}}, \quad (20)$$

gives the Matrix Formalism representation of the solution to the Bloch-Torrey PDE for the PGSE sequence. Denoting $\Phi = (\phi_1, \dots, \phi_{N_{\text{eig}}})^\top$ the vector of Laplace eigenfunctions and $\nu = \int_{\Omega} \rho(\mathbf{x}) \Phi(\mathbf{x}) d\Omega(\mathbf{x})$ the coefficients of the initial spin density in the Laplace eigenfunction basis, the magnetization at the end of the gradient sequence is given by

$$M^{\text{MF}}(\mathbf{x}, T_e) = \Phi^\top(\mathbf{x}) \mathbf{H}(\mathbf{g}, f) \nu. \quad (21)$$

The corresponding signal is

$$S^{\text{MF}}(\mathbf{g}, f) = \Phi^\top \mathbf{H}(\mathbf{g}, f) \nu, \quad (22)$$

where $\Phi = \int_{\Omega} \Phi(\mathbf{x}) d\Omega(\mathbf{x})$. If the spin density ρ is uniform across compartments ($\rho_i = \rho$ for all i), then $\nu = \rho \Phi$. If, additionally, all the compartments are connected to the same domain through permeable membranes ($N_{\text{group}} = 1$), the expression simplifies to $S^{\text{MF}}(\mathbf{g}, f) = \rho |\Omega| H_{11}(\mathbf{g}, f)$, where H_{11} is the element in the first row and first column of \mathbf{H} , as only the constant eigenfunction remains after integrating ($\Phi = (\sqrt{|\Omega|}, 0, \dots, 0)^\top$).

We note that in Eq. (20), the matrix \mathbf{L} in the exponent is diagonal, and in this case, the matrix exponential is also diagonal. The notation $*$ denotes the matrix complex conjugate transpose. In order to calculate the non-diagonal matrix exponential $e^{-\delta \mathbf{K}}$ and its conjugate $e^{-\delta \mathbf{K}^*} = (e^{-\delta \mathbf{K}})^*$, the scaling and squaring method^{43,44} is used (the built-in matrix exponential function in MATLAB, `expm`, is called). For large N_{eig} or many gradient sequences (\mathbf{g}, f), it may also be beneficial to approximate the resulting vector $\mathbf{H}\nu$ without explicitly assembling the matrix \mathbf{H} at all, by computing the action of the matrix exponentials on the three successive vectors without computing the matrix exponentials themselves⁴⁵. This approach may be used in a future version of SpinDoctor, in particular for other sequences than PGSE. However, for the purpose of theoretical analysis later, here we explicitly diagonalize the matrix $\mathbf{K}(\mathbf{g})$,

$$\mathbf{K}(\mathbf{g}) = \mathbf{V} \mathbf{B} \mathbf{V}^{-1}, \quad (23)$$

where \mathbf{V} has the eigenvectors in the columns and \mathbf{B} has the eigenvalues on the diagonal. Then $e^{-\delta \mathbf{K}} = \mathbf{V} e^{-\delta \mathbf{B}} \mathbf{V}^{-1}$ and $e^{-\delta \mathbf{K}^*} = (\mathbf{V}^{-1})^* e^{-\delta \mathbf{B}^*} \mathbf{V}^*$, hence, $\mathbf{H}(\mathbf{g}, f)$ can be written as

$$\mathbf{H}(\mathbf{g}, f) = (\mathbf{V}^{-1})^* e^{-\delta \mathbf{B}^*} \mathbf{V}^* e^{-(\Delta - \delta) \mathbf{L}} \mathbf{V} e^{-\delta \mathbf{B}} \mathbf{V}^{-1}. \quad (24)$$

SpinDoctor²⁹ provides built-in options of constructing geometries relevant to the brain white matter, including

1. spherical cells with a nucleus;
2. cylindrical cells with a myelin layer;
3. an extra-cellular space enclosed either a) in a box or b) in a tight wrapping around the cells;
4. deformation of canonical cells by bending and twisting;
5. permeable membranes;

The partial differential equations are solved by P_1 finite elements (the space of continuous piecewise linear functions on tetrahedral elements) combined with built-in MATLAB routines for solving ordinary differential equations (ODEs). The finite element mesh generation is performed using an external package called Tetgen⁴⁶. Each finite element mesh consists of

1. a list of N_{node} nodes in three dimensions: $(\mathbf{q}_1, \dots, \mathbf{q}_{N_{\text{node}}}) = (\mathbf{q}^x, \mathbf{q}^y, \mathbf{q}^z)^T \in \mathbb{R}^{3 \times N_{\text{node}}}$;
2. a list of N_{element} tetrahedral elements ($4 \times N_{\text{element}}$ indices referencing the nodes).

The list of nodes includes double nodes that are placed at the interfaces between compartments connected by permeable membranes. This allows for representing discontinuous magnetization fields M_i and M_j (or ϕ^i and ϕ^j) on the same boundary Γ_{ij} . To distinguish between the different compartments, let $\{1, \dots, N_{\text{node}}\} = \bigcup_{i=1}^{N_{\text{cpt}}} \mathcal{I}_i$ with $\mathcal{I}_i \cap \mathcal{I}_j = \emptyset$ for $i \neq j$. The set \mathcal{I}_i contains the indices of the nodes representing compartment Ω_i , including interface nodes. In the adjacent compartments, the corresponding interface nodes will have different indices, distinct from \mathcal{I}_i .

In SpinDoctor²⁹, the finite element space is the space of compartment-wise continuous piecewise linear functions on tetrahedral elements in three dimensions. This space has a set of basis functions whose number is exactly the number of finite element nodes (including double nodes), and that are defined on the entire domain Ω :

$$\varphi_k : \Omega \rightarrow [0, 1], \quad k \in \{1, \dots, N_{\text{node}}\}.$$

Let the finite element nodes be denoted by $\mathbf{q}_1, \dots, \mathbf{q}_{N_{\text{node}}}$. The basis function φ_k , $k \in \mathcal{I}_i$, is a piece-wise linear function, non-zero on the tetrahedra of Ω_i that touch the node \mathbf{q}_k , and zero on all other tetrahedra (including tetrahedra of other compartments different than Ω_i that do touch \mathbf{q}_k). At the interface Γ_{ij} between two compartments, the value of φ_k is set to be the value it has inside its own compartment, distinct from that of the adjacent compartment. On a tetrahedron of Ω_i that touches \mathbf{q}_k , φ_k is equal to 1 on \mathbf{q}_k and it is equal to 0 on the other 3 vertices of the tetrahedron. This completely describes the piece-wise linear function. The index sets may then be defined by $\mathcal{I}_i = \{k = 1, \dots, N_{\text{node}} \mid \text{supp}(\varphi_k) \subset \Omega_i\}$, the set of indices of the finite element nodal functions whose supports lie entirely within Ω_i .

Any function u in the finite element space can be written as a linear combination of the above basis functions:

$$u(\mathbf{x}) = \sum_{k=1}^{N_{\text{node}}} \alpha_k \varphi_k(\mathbf{x}) = \boldsymbol{\alpha}^T \boldsymbol{\varphi}(\mathbf{x}),$$

where $\boldsymbol{\alpha} = (\alpha_1, \dots, \alpha_{N_{\text{node}}})^T$ is the vector of coefficients and $\boldsymbol{\varphi} = (\varphi_1, \dots, \varphi_{N_{\text{node}}})^T$ is the vector of finite element nodal basis functions.

3.1 | Finite element discretization of the Laplace operator

To discretize the Laplace operator with permeable boundary conditions on the membranes of the biological cells, we construct the following finite element matrices: $\mathbf{M}, \mathbf{S}, \mathbf{Q} \in \mathbb{R}^{N_{\text{node}} \times N_{\text{node}}}$, known in the FEM literature as the mass, stiffness, and flux matrices, respectively. They are defined as

follows, for $(k, l) \in \{1, \dots, N_{\text{node}}\}^2$:

$$M_{kl} = \int_{\Omega} \varphi_k(\mathbf{x}) \varphi_l(\mathbf{x}) \, d\Omega(\mathbf{x}), \quad (25)$$

$$S_{kl} = \begin{cases} \int_{\Omega} D_i \nabla \varphi_k(\mathbf{x}) \cdot \nabla \varphi_l(\mathbf{x}) \, d\Omega(\mathbf{x}), & (k, l) \in \mathcal{I}_i^2, \quad i \in \{1, \dots, N_{\text{cmpt}}\}, \\ 0, & \text{otherwise,} \end{cases} \quad (26)$$

$$Q_{kl} = \sum_{i=1}^{N_{\text{cmpt}}} \sum_{j=1}^{N_{\text{cmpt}}} Q_{kl}^{ij}, \quad (27)$$

the last being defined as the sum of interface integrals:

$$Q_{kl}^{ij} = \begin{cases} \kappa_{ij} c_{ji} \int_{\Gamma_{ij}} \varphi_k(\mathbf{x}) \varphi_l(\mathbf{x}) \, d\Gamma(\mathbf{x}), & (k, l) \in \mathcal{I}_i^2, \\ -\kappa_{ij} c_{ij} \int_{\Gamma_{ij}} \varphi_k(\mathbf{x}) \varphi_l(\mathbf{x}) \, d\Gamma(\mathbf{x}), & (k, l) \in \mathcal{I}_i \times \mathcal{I}_j, \quad (i, j) \in \{1, \dots, N_{\text{cmpt}}\}^2. \\ 0, & \text{otherwise,} \end{cases} \quad (28)$$

Note that the above formulation correctly accounts for corner nodes (if any) that belong to two different permeable boundaries. We also remind the reader that i and j are compartment indices, while k and l are finite element nodal indices (representing the degrees of freedom for P_1 -elements).

The finite element discretization described above changes the continuous Laplace operator eigenvalue problem (10) to the following discrete, generalized *matrix* eigenvalue problem: find $(\lambda, \mathbf{p}) \in \mathbb{R} \times \mathbb{R}^{N_{\text{node}}}$ such that

$$\lambda \mathbf{M} \mathbf{p} = (\mathbf{S} + \mathbf{Q}) \mathbf{p}, \quad (29)$$

of which we will retain the N_{eig} smallest eigenvalues and corresponding eigenvectors $\{(\lambda_n, \mathbf{p}_n)\}_{1 \leq n \leq N_{\text{eig}}}$, with $N_{\text{eig}} \leq N_{\text{node}}$. Note however that there are in total N_{node} solutions to the problem (29). Moving back to the space of functions (the function space P_1), the eigenfunction $\phi_n(\mathbf{x})$ associated to the eigenvalue λ_n is then

$$\phi_n(\mathbf{x}) = \sum_{k=1}^{N_{\text{node}}} p_n^k \varphi_k(\mathbf{x}) = \mathbf{p}_n^T \boldsymbol{\varphi}(\mathbf{x}), \quad n \in \{1, \dots, N_{\text{eig}}\},$$

where the entries of the eigenvector \mathbf{p}_n are the coefficients of the eigenfunction ϕ_n in the finite element basis. Using matrix notation, this conversion can also be written $\phi = \mathbf{P}^T \boldsymbol{\varphi}$, where $\boldsymbol{\varphi} = (\varphi_1, \dots, \varphi_{N_{\text{node}}})^T$, $\phi = (\phi_1, \dots, \phi_{N_{\text{eig}}})^T$, and $\mathbf{P} = (\mathbf{p}_1, \dots, \mathbf{p}_{N_{\text{eig}}}) \in \mathbb{R}^{N_{\text{node}} \times N_{\text{eig}}}$. The integrals of the finite element discretized eigenfunctions are then given by $\Phi = \int_{\Omega} \phi(\mathbf{x}) \, d\Omega(\mathbf{x}) = \mathbf{P}^T \mathbf{M} \mathbf{o}$, where $\mathbf{o} = (1, \dots, 1)^T \in \mathbb{R}^{N_{\text{node}}}$. Similarly, the coefficients of the initial spin density in the finite element discretized eigenfunction basis are given by $\boldsymbol{\nu} = \int_{\Omega} \rho(\mathbf{x}) \phi(\mathbf{x}) \, d\Omega(\mathbf{x}) = \mathbf{P}^T \mathbf{M} \boldsymbol{\rho}$, where $\boldsymbol{\rho} = (\rho_{i(k)})_{1 \leq k \leq N_{\text{node}}} \in \mathbb{R}^{N_{\text{node}}}$ and $i(k) \in \{1, \dots, N_{\text{cmpt}}\}$ is such that $k \in \mathcal{I}_{i(k)}$.

In our previous work³⁷, we depended on the Partial Differential Equation Toolbox of MATLAB to solve the generalized eigenvalue problem in Eq. (29), but this is no longer needed in our current implementation. The MATLAB syntax `[P, lambda] = eigs(S + Q, M, Neig, "smallestreal", "IsSymmetricDefinite", true)` directly computes the N_{eig} smallest eigenvalues $\boldsymbol{\lambda} = (\lambda_1, \dots, \lambda_{N_{\text{eig}}})$ and eigenfunction nodal coordinates $\mathbf{P} = (\mathbf{p}_1, \dots, \mathbf{p}_{N_{\text{eig}}})$ using an iterative algorithm, given the mass, stiffness, and flux matrices \mathbf{M} , \mathbf{S} , and \mathbf{Q} . The built-in MATLAB command `eigs`^{47,48} can exploit the symmetry of \mathbf{M} and compute a subset of all the eigenvalues, meaning N_{eig} can be much smaller than N_{node} . Note that since the `eigs` command computes normalized vectors, we have to renormalize the resulting finite element *functions*. This is done as follows: if $\tilde{\mathbf{p}}$ is a normalized eigenvector of Eq. (29), i.e. $\|\tilde{\mathbf{p}}\|_2^2 = \sum_{k=1}^{N_{\text{node}}} \tilde{p}_k^2 = 1$, we define $\mathbf{p} = \frac{\tilde{\mathbf{p}}}{\sqrt{\tilde{\mathbf{p}}^T \mathbf{M} \tilde{\mathbf{p}}}}$. Then the squared L^2 -norm of the associated eigenfunction $\phi = \mathbf{p}^T \boldsymbol{\varphi}$ is given by $\|\phi\|_2^2 = \int_{\Omega} \phi^2(\mathbf{x}) \, d\Omega(\mathbf{x}) = \int_{\Omega} (\mathbf{p}^T \boldsymbol{\varphi}(\mathbf{x}))^2 \, d\Omega(\mathbf{x}) = \mathbf{p}^T \int_{\Omega} \boldsymbol{\varphi}(\mathbf{x}) \boldsymbol{\varphi}^T(\mathbf{x}) \, d\Omega(\mathbf{x}) \mathbf{p} = \mathbf{p}^T \mathbf{M} \mathbf{p} = 1$.

3.2 | Computation of first order moment product matrices

To obtain the Matrix Formalism signal representation, we must calculate the first order moments in the three coordinate directions of the product of pairs of eigenfunctions in Eq. (16-18). First, we define \mathbf{J}^x , \mathbf{J}^y , and \mathbf{J}^z ; the matrices containing the first order moments of the product of pairs of

finite element basis functions (where $\mathbf{x} = (x, y, z)^\top$):

$$J_{kl}^x = \int_{\Omega} x \varphi_k(\mathbf{x}) \varphi_l(\mathbf{x}) d\Omega(\mathbf{x}), \quad (k, l) \in \{1, \dots, N_{\text{node}}\}^2, \quad (30)$$

$$J_{kl}^y = \int_{\Omega} y \varphi_k(\mathbf{x}) \varphi_l(\mathbf{x}) d\Omega(\mathbf{x}), \quad (k, l) \in \{1, \dots, N_{\text{node}}\}^2, \quad (31)$$

$$J_{kl}^z = \int_{\Omega} z \varphi_k(\mathbf{x}) \varphi_l(\mathbf{x}) d\Omega(\mathbf{x}), \quad (k, l) \in \{1, \dots, N_{\text{node}}\}^2. \quad (32)$$

We note that in our previous work³⁷, our code contained a numerical implementation of \mathbf{J}^x , \mathbf{J}^y , and \mathbf{J}^z that had a slight error. We have since corrected this error and we now describe the correct implementation. The matrices \mathbf{J}^x , \mathbf{J}^y , and \mathbf{J}^z are assembled as coordinate weighted mass matrices, where the three coordinate functions $\mathbf{x} \mapsto x, y, z$ act as nodal weights in the assembly process, given by \mathbf{q}^x , \mathbf{q}^y , \mathbf{q}^z ; the vectors of x, y , and z coordinates of the finite element nodes. We refer to⁴⁹ for details about the matrix assembly. Then it is clear that the first order moments of the product of pairs of eigenfunctions can be written as:

$$A_{mn}^x = \int_{\Omega} x \phi_m(\mathbf{x}) \phi_n(\mathbf{x}) d\Omega(\mathbf{x}) = \mathbf{p}_m^\top \mathbf{J}^x \mathbf{p}_n, \quad (m, n) \in \{1, \dots, N_{\text{eig}}\}^2, \quad (33)$$

$$A_{mn}^y = \int_{\Omega} y \phi_m(\mathbf{x}) \phi_n(\mathbf{x}) d\Omega(\mathbf{x}) = \mathbf{p}_m^\top \mathbf{J}^y \mathbf{p}_n, \quad (m, n) \in \{1, \dots, N_{\text{eig}}\}^2, \quad (34)$$

$$A_{mn}^z = \int_{\Omega} z \phi_m(\mathbf{x}) \phi_n(\mathbf{x}) d\Omega(\mathbf{x}) = \mathbf{p}_m^\top \mathbf{J}^z \mathbf{p}_n, \quad (m, n) \in \{1, \dots, N_{\text{eig}}\}^2. \quad (35)$$

In the condensed form, we have $\mathbf{A}^u = \mathbf{P}^\top \mathbf{J}^u \mathbf{P}$, $u = x, y, z$. These matrices are computed using a total of six matrix-matrix multiplications. It is worth noting that while the three matrices \mathbf{J}^u are sparse, \mathbf{P} is dense.

3.3 | Eigenfunction length scale

On a line segment of length L and diffusivity D , the eigenvalues $(\lambda_1, \lambda_2, \dots)$ of the generalized Laplace operator with Neumann boundary conditions are

$$\lambda_n = \left(\frac{\pi(n-1)}{L} \right)^2 D, \quad n \in \mathbb{N}^*. \quad (36)$$

To make the link between the computed eigenvalue and the spatial scale of the eigenmode, we will convert the computed λ_n into a length scale (from the line segment eigenvalue formula):

$$L(\lambda) = \begin{cases} +\infty, & \lambda = 0, \\ \pi \sqrt{\frac{D}{\lambda}}, & \lambda > 0, \end{cases} \quad (37)$$

and characterize the computed eigenmode by $L(\lambda_n)$ instead of λ_n . The reference diffusivity $D = |\Omega|^{-1} \sum_{i=1}^{N_{\text{cmt}}} |\Omega_i| D_i$ is taken as a volume weighted mean of the diffusion coefficients $(D_i)_{1 \leq i \leq N_{\text{cmt}}}$.

We do not want to use the entire set of eigenvalues and eigenvectors $\{(\lambda_n, \mathbf{p}_n)\}_{1 \leq n \leq N_{\text{node}}}$ of the matrix eigenvalue problem in Eq. (29), because the size of \mathbf{M} , \mathbf{S} , and \mathbf{Q} is determined by the finite element discretization (it is equal to N_{node} , the number of finite element nodes). This means that most of the rapidly oscillating eigenmodes in the matrix eigenvalue problem are linked to the finite element discretization, and not to the physics of the problem. To link with the physics of the diffusion in the cell geometry, we set a restricted interval in which to keep the computed eigenvalues. We set the interval to be $[0, (\pi/L_{\text{min}})^2 D]$, where L_{min} is the shortest length scale of interest in the cell geometry. In this way, the number of computed eigenmodes, N_{eig} , will be much smaller than N_{node} .

In order to choose the minimum eigenfunction length scale L_{min} , a characteristic length scale L_{char}^Ω for the geometry of interest should be defined. Some examples of characteristic length scales are the average or smallest axon diameter for a geometry of axons, the average or smallest neuron dendrite branch diameter (or length) for a neuron geometry, or possibly the diameter of the neuron cell body (soma). One approach to algorithmically determine a characteristic length scale based on the geometry is given by

$$L_{\text{char}}^\Omega = \min_{1 \leq i \leq N_{\text{cmt}}} \min_{\substack{\mathbf{d} \in \mathbb{R}^3 \\ \|\mathbf{d}\|=1}} \max_{(\mathbf{x}, \mathbf{y}) \in \Omega_i^2} |\mathbf{d}^\top (\mathbf{x} - \mathbf{y})|, \quad (38)$$

with \mathbf{d} going over all the directions in 3 dimensions, and \mathbf{x}, \mathbf{y} going over all points in compartment Ω_i . Given i and \mathbf{d} , the inner expression identifies the largest width of compartment Ω_i in the direction \mathbf{d} . For a geometry of cylinders with various diameters, the above expression will return exactly the smallest cylinder diameter (provided all the cylinders are longer than their diameter).

Another characteristic length scale may be determined from the diffusion term $-\nabla \cdot D \nabla$ in the BTPDE, for which the mean distance of displacement of water molecules is given by

$$L_{\text{char}}^D(T_e) = \sqrt{2dDT_e}, \quad (39)$$

where $d = 3$ is the spatial dimension, and $D = |\Omega|^{-1} \sum_{i=1}^{N_{\text{cmt}}} |\Omega_i| D_i$. A third characteristic length scale is given by the shortest wavelength of the oscillations induced by second term $\dot{\gamma} f(t) \mathbf{g} \cdot \mathbf{x}$ in the BTPDE:

$$L_{\text{char}}^{\text{wave}}(\mathcal{G}, \mathcal{D}) = \left(\max_{\substack{\mathbf{g} \in \mathcal{G} \\ \delta \in \mathcal{D}}} \gamma \|\mathbf{g}\| \delta \right)^{-1}, \quad (40)$$

where \mathcal{G} and \mathcal{D} are the ranges of possible gradients and pulse durations to be considered. Note that this definition require upper bounds for the possible gradient amplitudes $\|\mathbf{g}\|$ and pulse durations δ . If such information is available, we may set $L_{\text{char}} = \min\{L_{\text{char}}^\Omega, L_{\text{char}}^D, L_{\text{char}}^{\text{wave}}\}$. Note also that the discretization of Ω presents a characteristic length scale given by the average tetrahedral diameter for the given mesh. This number should at least be smaller than the length scales given above, otherwise the mesh would not be sufficiently refined to accurately represent the solution to the BTPDE.

Once the characteristic length scale has been defined, the minimum eigenfunction length scale can then be expressed as a scaled version of the characteristic length scale. It is currently unclear what an appropriate scaling factor would be. However, using $L_{\text{min}} \sim L_{\text{char}}$ or $L_{\text{min}} \sim L_{\text{char}}/10$ as a first guess, one can compare the obtained matrix formalism signal with solutions that are known to be accurate for a few of the highest gradient amplitudes in some directions in order to choose the right length scale. Given a computational budget, one could directly solve the BTPDE for this comparison, choosing a length scale L_{min} giving satisfactory relative errors for the sequences considered. After that one may launch computations with an arbitrary number of gradient amplitudes, sequences, and directions based on the obtained length scale to compute the matrix formalism signal.

The MATLAB command `eigs` can identify the N_{eig} smallest eigenvalues of the problem in Eq. (29). If we choose this number to be large enough such that $L(\lambda_{N_{\text{eig}}}) \leq L_{\text{min}}$, we can be sure to have found all the modes of interest. If $N_{\text{eig}} \geq N_{\text{node}}/2$, the `eig` command is called instead, and a full decomposition is performed. In both cases, we only retain the eigenvalues whose length scales are larger than L_{min} to compute the Matrix Formalism signal. In order to find the number N_{eig} , we can either make a conservative estimate (of the order of N_{node}), and then remove the largest eigenvalues, or we can start out with a smaller first guess for N_{eig} and increment it if the smallest length scale obtained is too large. In particular, having identified the correct number of eigenmodes for a given set of parameters, this number can serve as a new first guess if we change the model parameters (diffusivity D , permeability κ).

4 | RESULTS

The simulations were performed on four multi-compartment geometries, denoted by Ω^{sphere} , Ω^{cyl} , Ω^{twist} , and Ω^{flat} . The geometries are shown in Figure 1 (the renderings were made in in Paraview^{50,51}). The multilayered sphere and cylinder (Ω^{sphere} and Ω^{cyl}) have rotational invariances that allow for comparing with known analytical solutions. The twisted geometry of 30 axons with an ECS (Ω^{twist}) allows for more complex interactions between the cells, with large intercellular surface areas. The axons were twisted to break some of the vertical invariance. Finally, the flat geometry of 30 axons and an ECS (Ω^{flat}) allows for further visualisation and study of diffusion in the plane. The curved outer boundaries illustrate the nature of the prescribed boundary conditions.

The geometries were generated with SpinDoctor as in²⁹. SpinDoctor creates the cell configuration and surface triangulation, while the finite element mesh is generated by an external package called Tetgen⁴⁶. The refinement parameter H controls the maximum volume of the tetrahedra, and is given in μm^3 .

The multilayered sphere and cylinder (Ω^{sphere} and Ω^{cyl}) both have inner, outer, and ECS radii of $r^{\text{in}} = 3.0\mu\text{m}$, $r^{\text{out}} = 5.0\mu\text{m}$, and $r^{\text{ecs}} = 7.5\mu\text{m}$ respectively, with the cylinder having a height of $h = 50.0\mu\text{m}$. Three refinement levels were used, resulting in 1492, 3523, and 8023 nodes for Ω^{sphere} , and 4674, 10626, and 19755 nodes for Ω^{cyl} . The coarsest and finest meshes are shown in Figure 1. Note that for Ω^{sphere} , the coarser mesh only has one interior point in the innermost compartment, and no interior points in the outer compartments. This is also the case for each slice of the coarser mesh of Ω^{cyl} .

The cylinders in the twisted geometry Ω^{twist} have radii ranging from $2\mu\text{m}$ to $6\mu\text{m}$, and a height of $h = 50\mu\text{m}$. Their centers were chosen randomly, and then manually repositioned to obtain a more compact configuration. A tight wrap ECS encloses the cylinders. After generating the finite element mesh, the nodes were gradually twisted along the vertical axis to an angle of $\pi/4$, thus breaking the axial invariance. Because the deformation was applied gradually, the quality of the tetrahedral elements was not reduced by any significance. One refinement level was used, with $H = 0.5\mu\text{m}^3$.

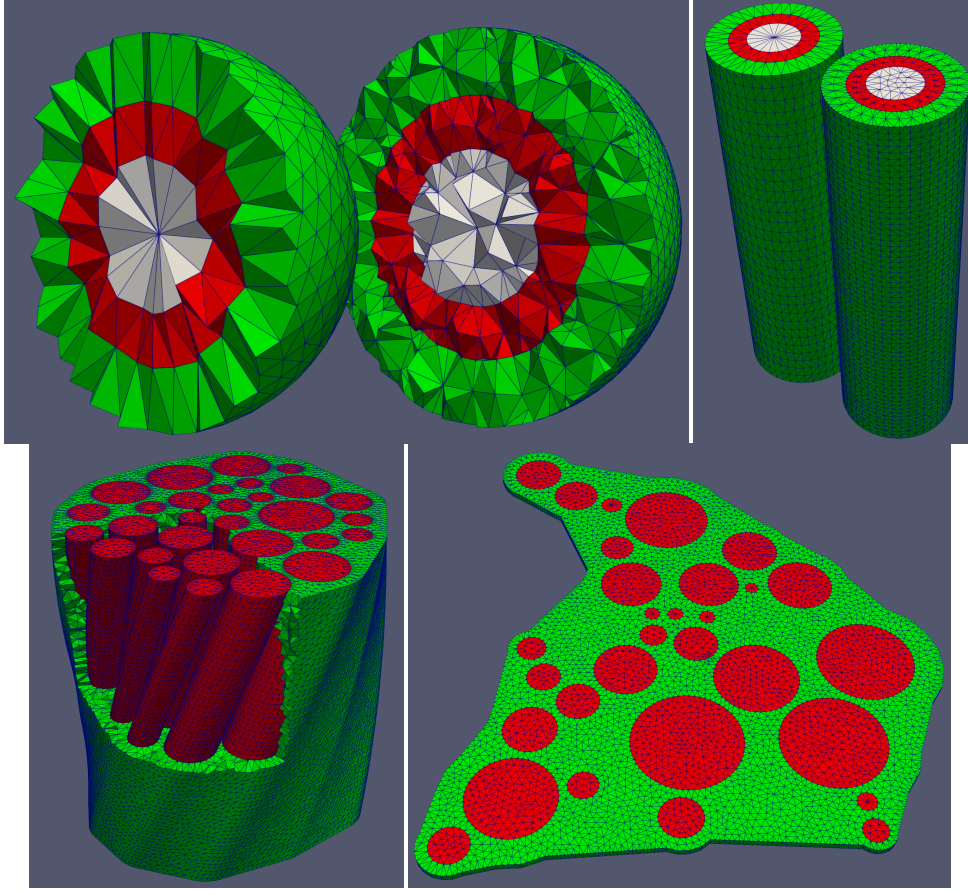


FIGURE 1 Finite element meshes of the different geometries used in the simulations. In order of appearance: Multilayered sphere (Ω^{sphere}), multilayered cylinder (Ω^{cyl}), thirty twisted axons (Ω^{twist}), and a section of thirty different axons (Ω^{flat}). The inner compartments are shown in white and red while the ECS-compartment is shown in green. For the multilayered cells, two different refinement levels are shown, with the coarser mesh being to the left in each image. Some geometries are clipped, to show the structure of the inner compartments. The geometries were visualized in Paraview.

The resulting mesh has 146002 nodes (including 95884 unique nodes) and 541957 tetrahedral elements. This means that the about 52.3% of the unique nodes lie on an intercompartment interface (not on the outer boundary). It is worth noting that this percentage would go to zero if the mesh was infinitely refined.

For the horizontal section geometry Ω^{flat} , the cylinders were generated with height $1\mu\text{m}$, $z \in [-0.5\mu\text{m}, 0.5\mu\text{m}]$, and radii ranging from $1\mu\text{m}$ to $8\mu\text{m}$, randomly placed according to the algorithm in SpinDoctor. With gradient directions restricted to the horizontal plane, the results on this geometry are assumed to be representative of those obtained with a larger cylinder height, as diffusion only occurs horizontally. To investigate the effect of the refinement parameter, three values of H were used (see Figure 2):

1. $H = 0.5\mu\text{m}^3$ —this mesh has 13797 nodes (including 11084 unique nodes) and 35652 tetrahedral elements;
2. $H = 0.2\mu\text{m}^3$ —this mesh has 24692 nodes (including 20192 unique nodes) and 62335 tetrahedral elements;
3. $H = 0.1\mu\text{m}^3$ —this mesh has 40713 nodes (including 33845 unique nodes) and 114753 tetrahedral elements.

In order to compute the magnetization M and signal S , four approaches were used. The analytical matrix formalism solution is denoted by “analytical”, the Karger solution by “Karger”, the finite element discretized matrix formalism solution by “MF”, and the finite element discretized BTPDE solution by “BTPDE”. The last is given by $M^{\text{BTPDE}}(\mathbf{x}, t) = \boldsymbol{\xi}^T(t)\boldsymbol{\varphi}(\mathbf{x})$ for $\mathbf{x} \in \Omega$ (resulting in $S^{\text{BTPDE}} = \boldsymbol{\xi}^T(T_e) \int_{\Omega} \boldsymbol{\varphi}(\mathbf{x}) d\Omega(\mathbf{x})$), where $\boldsymbol{\xi} : [0, T_e] \rightarrow \mathbb{C}^{N_{\text{node}}}$ is the solution to the following equation:

$$\mathbf{M} \frac{d\boldsymbol{\xi}}{dt} = -(\mathbf{S} + \mathbf{Q} + i\gamma f(t)\mathbf{J}(\mathbf{g})) \boldsymbol{\xi}(t), \quad t \in [0, T_e] \quad (41)$$

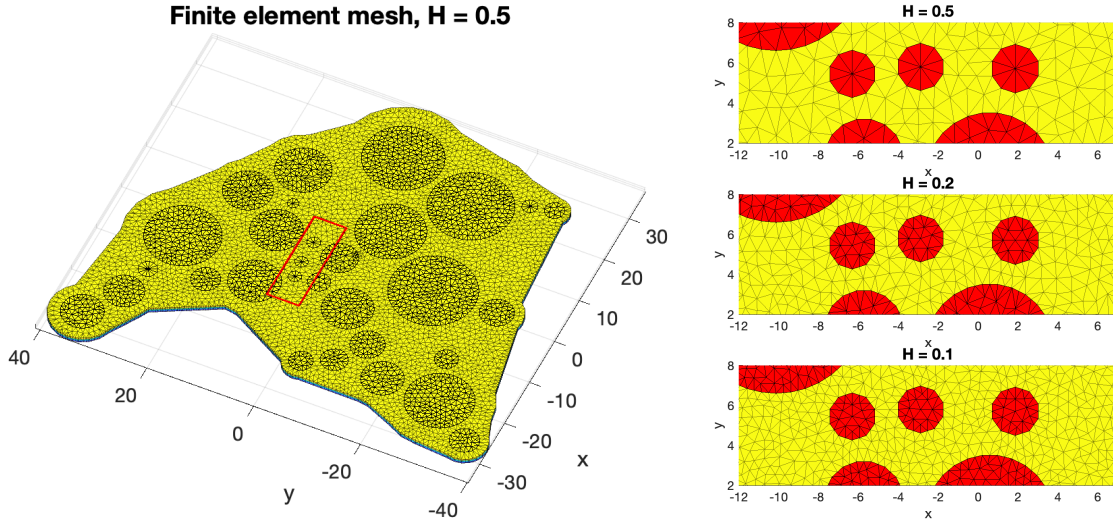


FIGURE 2 Finite element mesh of the geometry Ω^{flat} . The element size is controlled by the refinement parameter H . Left: finite element mesh for $H = 0.5\mu\text{m}^3$. Right: zoom on some of the smallest axons (red rectangle on the left) for different refinements. The units are $x, y, z : \mu\text{m}$, $H : \mu\text{m}^3$

with initial conditions $\xi_k(0) = \rho_{i(k)}$ for $k \in \{1, \dots, N_{\text{node}}\}$, where $i(k) \in \{1, \dots, N_{\text{cpt}}\}$ is such that $k \in \mathcal{I}_{i(k)}$. The above equation is solved in SpinDoctor with build-in MATLAB routines for ordinary differential equation (ODE) systems. The time stepping is controlled by setting the absolute and relative tolerances ϵ_{abs} and ϵ_{rel} of the MATLAB ODE solver `ode15s`⁵². We refer the reader to²⁹ for details on how to use SpinDoctor.

For each compartment, the diffusivity and initial spin density were set to the constant values $D = 0.002\text{mm}^2/\text{s}$ and $\rho = 1.0$, respectively. In the literature, most experimentally measured values of the permeability κ in biological cells range from 10^{-8}m/s to 10^{-4}m/s ⁵³. The case of impermeable membranes having been treated in our previous work, the simulations were mainly performed with values between 10^{-5}m/s and 10^{-4}m/s , with some simulations performed with $\kappa = 10^{-3}\text{m/s}$ to illustrate the mathematical correctness of the model for high permeabilities.

4.1 | Validation on known analytical solutions

For simple geometries, analytical solutions may be obtained for the BTPDE. In this section, we compare the MF and BTPDE solutions to analytical solutions for a 3-layered sphere and a 3-layered cylinder. The exact solutions were obtained by exploiting rotational symmetries so that the Laplace eigenvalue problem is decomposed into radial and angular parts, as presented in^{34,38}. An adapted version of the corresponding code was used. Two pulsed sequences ($\delta = 5\text{ms}$, $\Delta = 10\text{ms}$) and ($\delta = 10\text{ms}$, $\Delta = 100\text{ms}$) were considered, with b -values ranging from 0 to $10000\text{s}/\text{mm}^2$. The gradient direction was set to $\mathbf{g} = (1.0, 0.0, 0.0)^T$. The interface permeability was set to $\kappa = 10^{-4}\text{m/s}$. Different refinement levels were tested, as is illustrated in Figure 1.

We briefly describe our implementation of the analytical approach. The analytical solution uses the same matrix formalism approach as presented above, but decomposes the Laplace eigenfunctions into their radial and angular parts. The radial eigenvalues are obtained by finding the roots of a function. A dichotomy approach was used for this purpose, where the radial eigenvalue space is swept using an assumed minimal distance $\Delta\alpha$ between the square root α of the radial eigenvalues $\lambda^{\text{radial}} = \alpha^2$, for each angular eigenmode. The step was set to $\Delta\alpha^2 = 10^{-8}\mu\text{s}^{-1}$, and the correct identification of the roots was further confirmed by plotting the function. In addition, the number of eigenvalues was truncated using the length scale formula in Eq. (37), which was applied to the maximum radial eigenvalue to be kept, where the corresponding radial length scale was set to $L(\alpha_{\text{max}}^2) \geq L^{\text{radial}} = 0.3\mu\text{m}$. Values below this threshold were found to produce no significant difference in the obtained signal.

In order to choose the eigenvalue truncation for the finite element matrix formalism solutions, minimum length scales of $3\mu\text{m}$, $2\mu\text{m}$, and $1\mu\text{m}$ were tested. The results are shown in Figure 3. The finite element based matrix formalism has two main sources of error: finite element discretization and Laplace eigenfunction basis truncation. In contrast, the above multilayered formulation only has errors from the eigenfunction basis truncation, but these were negligible compared to the differences between the multilayered and finite element matrix formalism results.

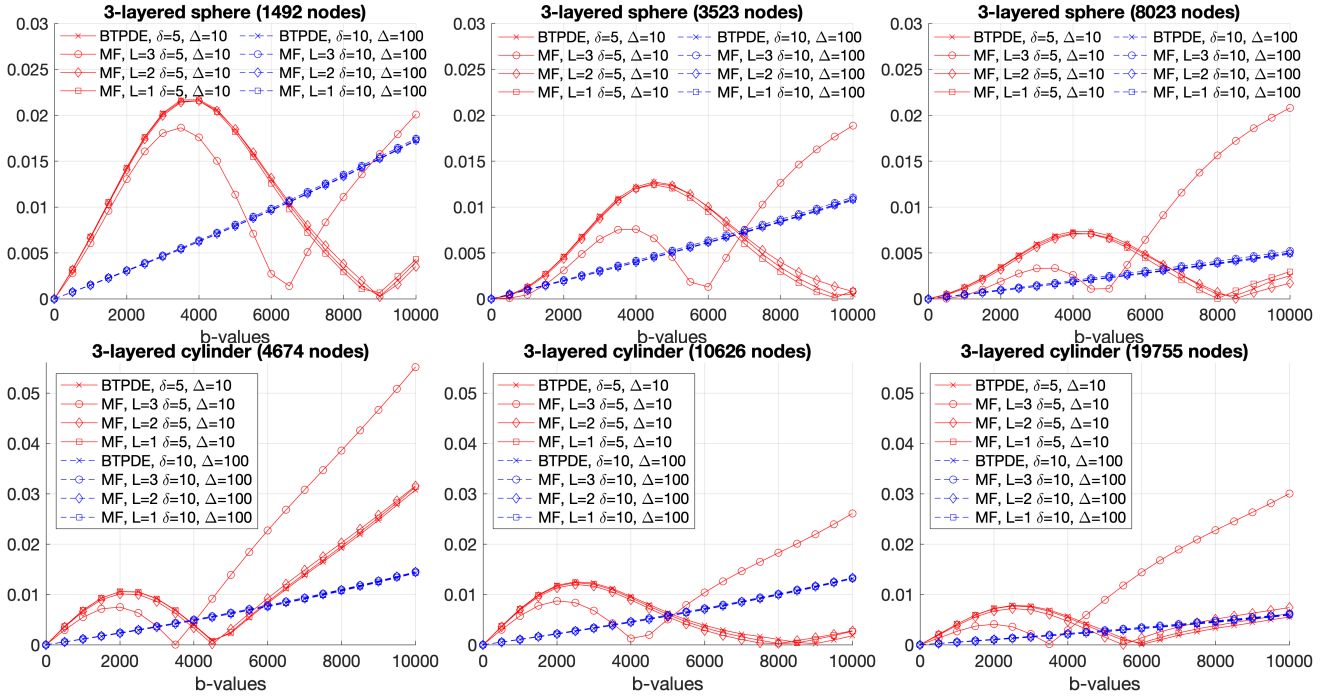


FIGURE 3 Relative errors $|S - S^{\text{analytical}}|/|S^{\text{analytical}}|$ (not in percent) for BTPDE and MF signals with respect to the truncated analytical multilayer MF signal. The first row is for the 3-layered sphere (Ω^{sphere}), and the second for the 3-layered cylinder (Ω^{cyl}). The units are $L : \mu\text{m}$, $\delta, \Delta : \text{ms}$, $b : \text{s}/\text{mm}^2$.

The errors decrease with the refinement level (as indicated by the number of nodes). However, the mesh quality is not uniquely determined by the number of nodes, as can be seen for Ω^{cyl} (bottom row). Here, in the middle column, the mesh still have few interior points (which is also the case for the coarse mesh). For the longer diffusion time, the errors increase linearly with the b-value for both BTPDE and MF, which is also expected. For the shorter diffusion times, higher gradient amplitudes are required to produce the same b-values, which results in a more variable error profile. The low errors observed for certain b-values can be due to resonance effects, where the magnetization oscillates with certain frequencies on the symmetrical geometry. While $L \in \{1\mu\text{m}, 2\mu\text{m}\}$ produces roughly the same errors as BTPDE, $L = 3\mu\text{m}$ has higher errors for larger b-values, but can also produce lower errors than the other length scales and BTPDE for lower b-values. This could be due to the length scale truncation acting as a low pass filter for the magnetization, reducing oscillations due to the finite element discretization.

4.2 | Validation of Matrix Formalism signal compared to the reference solution

For Ω^{flat} , the diffusion MRI signals are averaged over 64 gradient directions uniformly distributed on a unit semicircle in the horizontal plane to obtain a direction averaged signal:

$$S = \frac{1}{64} \sum_{d=1}^{64} S(f, \mathbf{g}_d). \quad (42)$$

where $\mathbf{g}_d = \|\mathbf{g}\| (\cos(\pi \frac{d}{64}), \sin(\pi \frac{d}{64}), 0)^{\text{T}}$.

To investigate the question of what range of Laplace eigenvalues is sufficient to accurately describe the diffusion MRI signal, we computed the Bloch-Torrey PDE signals S^{BTPDE} and the Matrix Formalism signals S^{MF} for different permeability coefficients $\kappa = 10^{-3} \text{m/s}, 10^{-5} \text{m/s}$ and different gradient amplitudes $\|\mathbf{g}\| = 0.075 \text{T/m}, 0.374 \text{T/m}$ on three finite element meshes with Tetgen refinement parameters $H = 0.5\mu\text{m}^3, 0.2\mu\text{m}^3, 0.1\mu\text{m}^3$. The ODE tolerances for S^{BTPDE} were $\epsilon_{\text{abs}} = 10^{-6}$ and $\epsilon_{\text{rel}} = 10^{-4}$.

The signal S^{BTPDE} on the finest mesh with $H = 0.1\mu\text{m}^3$ is considered the reference solution. The signal S^{MF} was computed for $H = 0.5\mu\text{m}^3, 0.2\mu\text{m}^3$ with two minimum length scales $L = 3\mu\text{m}, 2\mu\text{m}$. In Table 1, we show the mean relative error between the various simulations and the reference solution, averaged over the 64 gradient directions. Two gradient amplitudes and three PGSE sequences (with $\delta = \Delta = 5\text{ms}, 10\text{ms}, 20\text{ms}$) were simulated, making a range of b-values from $267\text{s}/\text{mm}^2$ to $53333\text{s}/\text{mm}^2$.

κ	$\ g\ $	δ	b	Reference BTPDE H0.1	Mean relative error (%)					
					BTPDE		MF			
					H0.5	H0.2	H0.5 L3	H0.5 L2	H0.2 L3	H0.2 L2
10^{-3}	0.075	10	267	0.676	0.05	0.01	0.06	0.07	0.03	0.03
		20	2133	0.084	0.41	0.13	0.53	0.55	0.25	0.26
10^{-3}	0.374	5	833	0.285	0.60	0.18	0.58	0.66	0.17	0.24
		10	6666	0.008	0.29	0.09	0.42	0.16	0.18	0.04
		20	53333	2.4e-4	0.93	0.25	1.35	0.65	0.55	0.05
10^{-5}	0.075	10	267	0.794	0.12	0.04	0.12	0.13	0.04	0.05
		20	2133	0.358	0.24	0.07	0.25	0.26	0.08	0.10
10^{-5}	0.374	5	833	0.449	0.41	0.12	0.32	0.42	0.03	0.14
		10	6666	0.098	0.19	0.10	0.50	0.22	0.44	0.13
		20	53333	0.031	0.95	0.43	2.21	1.13	1.81	0.62

TABLE 1 Relative errors $|S - S^{\text{ref}}|/|S^{\text{ref}}| \times 100$ (in percent) of S_H^{BTPDE} and $S_{H,L}^{\text{MF}}$ with respect to the reference signal S^{ref} for different refinements $H = 0.5\mu\text{m}^3, 0.2\mu\text{m}^3$ and length scales $L = 3\mu\text{m}, 2\mu\text{m}$. The geometry is on Ω^{flat} . The units are κ : m/s, $\|g\|$: T/m, δ : ms, b : s/mm², H : μm^3 and L : μm . The signal S^{BTPDE} on the finest mesh with $H = 0.1\mu\text{m}^3$ is considered the reference solution. For the reference signal, its normalized value S/S_0 is shown, where $S_0 = \rho|\Omega|$ is the signal for zero b-weighting. The signal is an averaged signal, taken over 64 gradient directions uniformly distributed on a unit semicircle in the horizontal plane. The two pulses were without a pause between them: $\delta = \Delta$. The geometry is Ω^{flat} .

The mean relative errors between the reference solution and S^{BTPDE} with $H = 0.2\mu\text{m}^3$ range from 0.01% to 0.43%. This implies the errors of the reference solution compared to the exact solution are in the same range. The mean relative error between the reference solution and S^{BTPDE} with $H = 0.5\mu\text{m}^3$ range between 0.05% and 0.95%. Concerning the MF solutions, on the $H = 0.5\mu\text{m}^3$ mesh, the mean relative errors ranged from 0.06% to 2.21% compared to the reference solution if $L = 3\mu\text{m}$ was chosen as the eigenvalue length scale limit, and the errors ranged from 0.07% to 1.13% if $L = 2\mu\text{m}$ was chosen as the eigenvalue length scale limit. On the finer mesh, $H = 0.2\mu\text{m}^3$, the errors ranged from 0.03% to 1.81% using the $L = 3\mu\text{m}$ eigenvalue limit, and the errors ranged from 0.03% to 0.62% using the $L = 2\mu\text{m}$ eigenvalue limit. The highest relative errors correspond to the cases with the highest b-values, for which the signal has the highest decay.

In Figure 4, the relative errors of the MF and BTPDE signals with respect to the BTPDE signal on the finest mesh are shown for different refinement levels and length scales. It is clear that the error decreases as the mesh becomes finer. In addition, once an error threshold is reached, decreasing the L limit, meaning increasing the number of computed eigenfunctions, does not necessarily further reduce the error beyond the level of the BTPDE signal for the same mesh. For lower b-values, higher length scales can be tolerated than for higher b-values. The MF errors may however drop below those of the BTPDE signals. This can be due to the time approximation of the MF signal being exact (for the PGSE sequence), while the time approximation for the BTPDE is done numerically (with relative and absolute tolerances $\epsilon_{\text{abs}} = 10^{-6}$ and $\epsilon_{\text{rel}} = 10^{-4}$).

In Table 2, the mean relative errors on Ω^{twist} over seven gradient directions are shown for the MF signal with respect to the BTPDE signal. Two permeabilities $\kappa = 10^{-4}$ and 10^{-5} m/s, two sequences $(\delta, \Delta) \in \{(5\text{ms}, 5\text{ms}), (10\text{ms}, 50\text{ms})\}$, and four b-values $b = 1000, 3000, 7000,$ and 10000s/mm^2 were used, fixing the number of eigenvalues to 2000 and 3500, resulting in length scales between $3.754\mu\text{m}$ and $2.901\mu\text{m}$. For the longer sequences, the errors were of the order of 0.1% or lower for $N_{\text{eig}} = 2000$, and between 0.01% and 0.03% for $N_{\text{eig}} = 3500$. This suggests that a smaller number of eigenvalues may be sufficient to represent the signal at a precision of 1%. At equivalent b-value, the shorter sequence requires a much stronger gradient ($\|g\| = 1.295\text{T/m}$ for $b = 10000\text{s/mm}^2$), resulting in high frequency oscillations that were not caught for $N_{\text{eig}} = 2000$. This can be seen for the high errors of 12% and 24%. Increasing the number of eigenfunctions to $N_{\text{eig}} = 3500$ did however provide a sufficient number of high wavenumber modes to correctly represent the signal, producing errors below 1%.

4.3 | Comparing with the Karger model

The Karger model^{54,55} computes the compartment magnetizations for narrow pulses. A recent extension of the Karger model to finite pulses is the Finite Pulse Karger model (FPK)⁵⁶. Here we numerically compare the direction averaged signal attenuation of the BTPDE and MF solution to the FPK solution on Ω^{twist} . The results are shown in Figure 5. The signal was computed in seven uniformly distributed directions on the sphere,

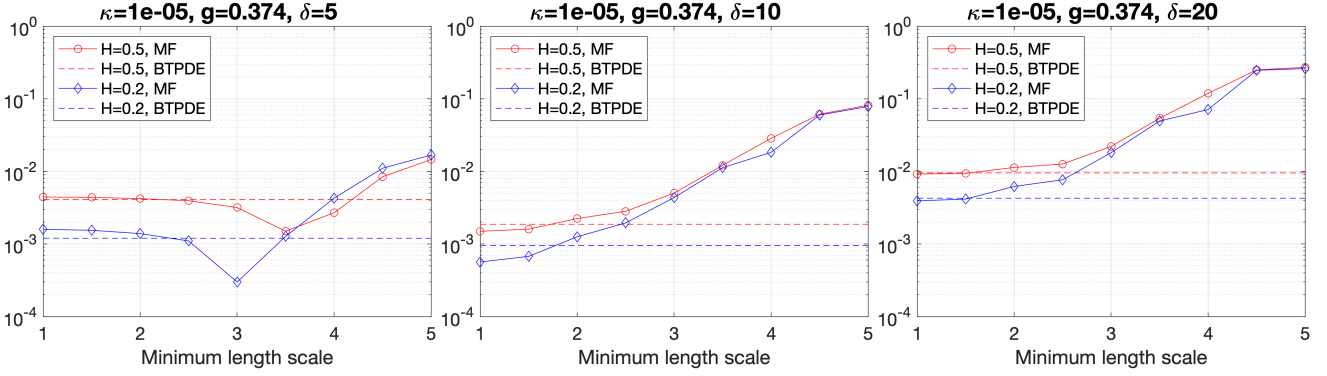


FIGURE 4 Relative errors $|S - S^{\text{ref}}|/|S^{\text{ref}}|$ (not in percent) for MF and BTPDE compared to the reference signal (64 directions averaged), with $\delta = \Delta$. The geometry is Ω^{flat} . The signal S^{BTPDE} on the finest mesh with $H = 0.1 \mu\text{m}^3$ is considered the reference solution. The MF error is plotted for different length scales. The units are κ : m/s, $\|g\|$: T/m, δ : ms, H : μm^3 , length scales μm .

κ	δ	Δ	b	$\ g\ $	$\frac{ S^{\text{BTPDE}} }{ S_0 }$	MF mean relative error (%)	
						$N_{\text{eig}} = 2000$	$N_{\text{eig}} = 3500$
10^{-4}	5	5	1000	0.409	0.334	0.559	0.109
			3000	0.819	0.045	4.892	0.242
			7000	1.083	0.018	12.687	0.411
			10000	1.295	0.010	24.440	0.604
10^{-4}	10	50	1000	0.055	0.438	0.018	0.007
			3000	0.109	0.076	0.052	0.018
			7000	0.145	0.028	0.066	0.026
			10000	0.173	0.016	0.073	0.031
10^{-5}	5	5	1000	0.409	0.374	0.643	0.104
			3000	0.819	0.070	5.060	0.203
			7000	1.083	0.031	12.549	0.366
			10000	1.295	0.018	23.997	0.547
10^{-5}	10	50	1000	0.055	0.513	0.021	0.006
			3000	0.109	0.181	0.067	0.012
			7000	0.145	0.114	0.108	0.015
			10000	0.173	0.084	0.154	0.018

TABLE 2 Relative errors $|S_L^{\text{MF}} - S^{\text{BTPDE}}|/|S^{\text{BTPDE}}| \times 100$ (in percent) of S_L^{MF} with respect to S^{BTPDE} . The geometry is Ω^{twist} . The MF parameters are $N_{\text{eig}} \in \{2000, 3500\}$, resulting in $L \in \{3.754 \mu\text{m}, 2.954 \mu\text{m}\}$ respectively for $\kappa = 10^{-5}$, and $L \in \{3.662 \mu\text{m}, 2.901 \mu\text{m}\}$ for $\kappa = 10^{-4}$. The units are κ : m/s, $\|g\|$: T/m, δ : ms, b : s/mm², H : μm^3 and L : μm . For the reference signal, its normalized value $|S^{\text{BTPDE}}|/|S_0|$ is shown, where $S_0 = \rho|\Omega|$ is the signal for zero b -weighting. The signal is an averaged signal, taken over 7 gradient directions uniformly distributed on the unit sphere.

two gradient sequences $(\delta, \Delta) \in \{(5\text{ms}, 5\text{ms}), (10\text{ms}, 50\text{ms})\}$, and b -values ranging from 0s/mm^2 to 4000s/mm^2 (11 values for MF and BTPDE, 51 values for FPK). For the MF signal, $N_{\text{eig}} = 3500$ eigenvalues were used, resulting in a minimum length scale of $L = 2.954 \mu\text{m}$. While the MF and BTPDE (reference) signal attenuations are indiscernible, the FPK signal attenuations are slightly stronger for higher b -values.

For each compartment Ω_i , $i \in \{1, \dots, 31\}$ ($N_{\text{cmt}} = 31$ for Ω^{twist}), the six components of the symmetric diffusion tensor for the FPK model,

$$\mathbf{D}_i = \begin{pmatrix} D_i^{xx} & D_i^{xy} & D_i^{xz} \\ D_i^{xy} & D_i^{yy} & D_i^{yz} \\ D_i^{xz} & D_i^{yz} & D_i^{zz} \end{pmatrix},$$

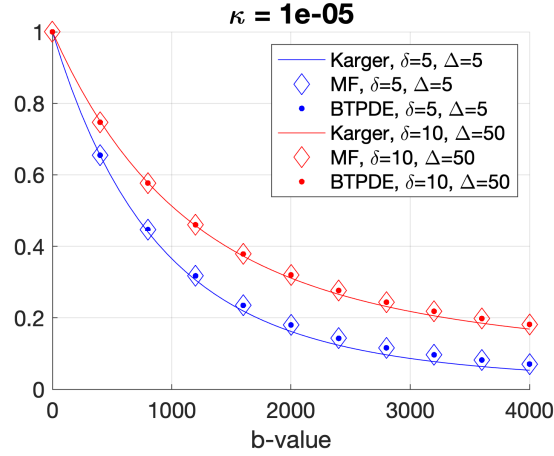


FIGURE 5 Signal attenuation $|S|/|S_0|$ for the BTPDE, MF, and Karger signals, averaged over 7 uniformly distributed directions in three dimensions. The geometry is Ω^{twist} . The permeability is $\kappa = 10^{-5}$ m/s. The units are κ : m/s, δ, Δ : ms, b : s/mm². There are 11 b -values for BTPDE and MF, and 51 b -values for Karger. The Karger signals were computed after fitting a diffusion tensor to each compartment and diffusion time using a homogenized apparent diffusion coefficient model.

were fitted using a least squares approach to apparent diffusion coefficients computed using a homogenized model⁵⁷ (HADC) in 50 uniformly distributed directions on the unit sphere. One set of diffusion tensors was fitted for each diffusion time scale. The two sets of diffusion tensors, $(\mathbf{D}_i^{\text{short}})_{1 \leq i \leq 31}$ and $(\mathbf{D}_i^{\text{long}})_{1 \leq i \leq 31}$, differ by the diffusion time (short: $(\delta, \Delta) = (5\text{ms}, 5\text{ms})$; long: $(\delta, \Delta) = (10\text{ms}, 50\text{ms})$). Below we present the obtained volume-averaged axon diffusion tensor

$$\mathbf{D}_{\text{axon}} = \frac{\sum_{i=1}^{30} |\Omega_i| \mathbf{D}_i}{\sum_{i=1}^{30} |\Omega_i|}$$

and the ECS-diffusion tensor $\mathbf{D}_{\text{ECS}} = \mathbf{D}_{31}$ for both diffusion times, as a fraction of the intrinsic diffusivity $D = 0.002\text{mm}^2/\text{s}$:

$$\mathbf{D}_{\text{axon}}^{\text{short}} = \begin{pmatrix} 0.249 & 0.001 & 0.013 \\ 0.001 & 0.247 & -0.006 \\ 0.013 & -0.006 & 0.839 \end{pmatrix} \times D, \quad \mathbf{D}_{\text{ECS}}^{\text{short}} = \begin{pmatrix} 0.585 & -0.017 & 0.007 \\ -0.017 & 0.587 & -0.004 \\ 0.007 & -0.004 & 0.865 \end{pmatrix} \times D,$$

$$\mathbf{D}_{\text{axon}}^{\text{long}} = \begin{pmatrix} 0.041 & 0.002 & 0.007 \\ 0.002 & 0.042 & -0.008 \\ 0.007 & -0.008 & 0.650 \end{pmatrix} \times D, \quad \mathbf{D}_{\text{ECS}}^{\text{long}} = \begin{pmatrix} 0.480 & -0.019 & 0.006 \\ -0.019 & 0.482 & -0.004 \\ 0.006 & -0.004 & 0.673 \end{pmatrix} \times D.$$

A component of $1.000 \times D$ would signify that the diffusion in the associated direction is unhindered by the cell membranes. For the shorter diffusion time, fewer water molecules interact with the cell membranes, as the average distance travelled by the molecules is shorter. As a result, the components are closer to the intrinsic diffusivity than for the longer diffusion time. For both diffusion times, the vertical component D^{zz} is larger than the other components, which indicates that diffusion in the vertical direction (z -direction) is privileged. Even after twisting the geometry, the axons are still mostly oriented along the vertical axis. In contrast, the ECS-compartment ($i = 31$) presents less of a difference on the diagonal, as diffusion in the horizontal plane is less hindered (the molecules can travel freely around the smaller axons). While the tensors may contain negative values in the off-diagonal components, they all remain positive definite.

4.4 | Permeability effects on the magnetization solution

In this section, we analyze how the permeability coefficient affects the magnetization solution on Ω^{flat} , and the influence of the boundary curvature. The magnetization solutions were computed using the implementation of the Matrix Formalism method described previously. We computed the direction averaged magnetizations for two permeabilities $\kappa = 10^{-3}$ m/s, 10^{-5} m/s, two gradient amplitudes $\|g\| = 0.075\text{T/m}$, 0.374T/m and four PGSE sequences with $b = 200\text{s/mm}^2$, 1000s/mm^2 , 4000s/mm^2 , 10000s/mm^2 with their corresponding diffusion times for $\delta = \Delta$. At $\|g\| = 0.075\text{T/m}$, $\delta \in \{9.1\text{ms}, 15.5\text{ms}, 24.7\text{ms}, 33.5\text{ms}\}$, and at $\|g\| = 0.374\text{T/m}$, $\delta \in \{3.1\text{ms}, 5.3\text{ms}, 8.4\text{ms}, 11.4\text{ms}\}$.

The resulting magnetizations for $\kappa = 10^{-3}$ m/s are shown in Figure 6. When the permeability is high, as in the case of $\kappa = 10^{-3}$ m/s, the cell boundaries do not hinder the movement of the water molecules, and the domain behaves more like a homogeneous medium bounded only by

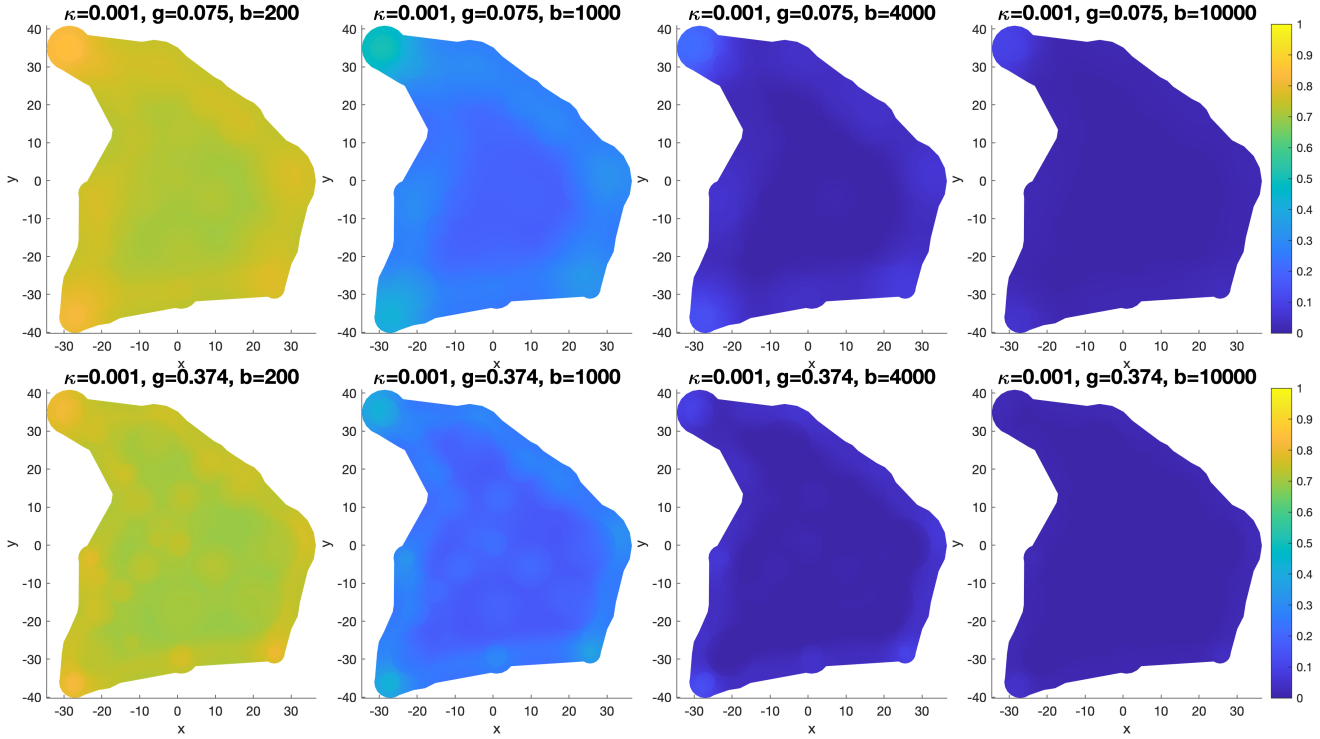


FIGURE 6 The 64 directions averaged magnetization on Ω^{flat} for two gradient amplitudes $\|g\|$ (rows) and four b -values (columns). The diffusion times were adjusted to obtain a constant b -value in each column. The permeability is $\kappa = 10^{-3}$ m/s. The units are κ : m/s, $\|g\|$: T/m, b : s/mm², x, y : μm . The magnetization is shown at the top layer ($z = 0.5\mu\text{m}$), but does not vary in the z -direction. Only the real part is plotted, as the complex part is insignificant in comparison.

the exterior boundary. The magnetization should thus depend mainly on the b -value, which combine the effects of the gradient amplitude and corresponding diffusion time. This does indeed seem to be the case in the figure. Additionally, the high curvature of the smallest axons does not seem to affect the solution. In the corners of the domain, which are enclosed by curved boundaries, and to a lesser extent near the outer wall in general, the attenuation is weaker, as the diffusion is restricted by the hard wall boundary conditions²⁷.

For the lower permeability ($\kappa = 10^{-5}$ m/s, see Figure 7), the magnetization attenuates less than for higher permeability at equivalent b -value. In addition, the magnetization varies significantly with the amplitude $\|g\|$ at equivalent b -value; this differs from the previous higher permeability example. The magnetization value is higher in the cells than in the ECS; and the smaller the cell, the higher the magnetization value. Compared to the high permeability example, the attenuation in the ECS is not only weak at the outer boundary, but also near the interior boundaries, which now behave more like hard walls.

In order to investigate further the magnetization value in the different compartments, we computed the direction-averaged magnetizations, normalized over the volume of each of the thirty cells of Ω^{flat} (excluding the ECS, with index $i = 31$),

$$\bar{M}_i = \frac{1}{\rho|\Omega_i^{\text{flat}}|} \int_{\Omega_i^{\text{flat}}} M(\mathbf{x}, T_e) d\Omega(\mathbf{x}), \quad i \in \{1, \dots, 30\}, \quad (43)$$

and plotted them against the cell volumes $|\Omega_i^{\text{flat}}|$ in Figure 8. This is done in order to examine how the compartment size affects the magnetization attenuation. For free diffusion with constant initial spin density, the integral of the final magnetization depends on the b -value alone. Its decay is given by $\bar{M} = e^{-Db}$, and does not depend on the integration domain. We can see that, for $\kappa = 10^{-3}$ m/s, the magnetization attenuates at the same rate in most of the compartments, which corresponds to a rather flat baseline curve for each b -value, as compared to the more restricted regime with lower permeability $\kappa = 10^{-5}$ m/s, whose magnetizations attenuate less in the smaller compartments. At $\kappa = 10^{-5}$ m/s, at higher cell volumes, the curve flattens, which can be attributed to unrestricted diffusion inside the big cells (away from the cell boundaries). In addition, at $\kappa = 10^{-3}$ m/s, we notice certain peaks in the curves, for example, at volumes $21.57\mu\text{m}^3$ and $44.17\mu\text{m}^3$. This is due to the diffusion being more restricted near the domain boundary, which is a hard wall. In particular, the two cells with volumes $21.57\mu\text{m}^3$ and $44.17\mu\text{m}^3$ correspond exactly to the two cells at two corners of the domain. Their large magnetizations can be attributed to the high curvature of the domain boundary around

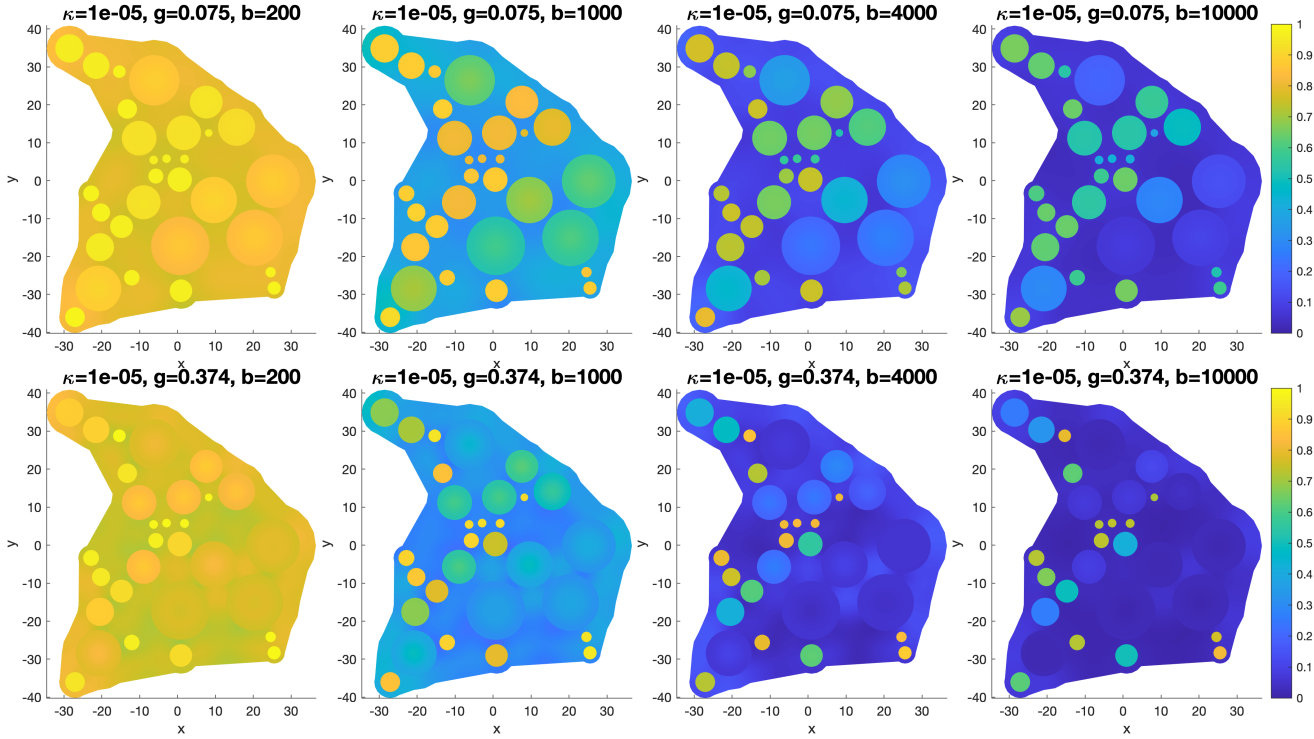


FIGURE 7 The 64 directions averaged magnetization on Ω^{flat} for two gradient amplitudes $\|g\|$ (rows) and four b -values (columns). The diffusion times were adjusted to obtain a constant b -value in each column. The permeability is $\kappa = 10^{-5} \text{ m/s}$. The units are $\kappa : \text{m/s}$, $\|g\| : \text{T/m}$, $b : \text{s/mm}^2$, $x, y : \mu\text{m}$. The magnetization is shown at the top layer ($z = 0.5 \mu\text{m}$), but does not vary in the z -direction. Only the real part is plotted, as the complex part is insignificant in comparison.

them, which restricts the outward diffusion. In essence, the hard wall condition on the computational boundary reflects the spins back into those two axons. As the permeability decreases, the magnetization inside each cell becomes less affected by the surrounding boundary-induced ECS magnetization, and more affected by their own boundary. For $\kappa = 10^{-5} \text{ m/s}$, the peaks are still visible, but only at the lower gradient amplitude. In addition, at $\kappa = 10^{-5}$, both very small axons and very large axons have lower magnetization than the middle range of axons. The reason is the following. In the very small axons, the spins enter and leave the axons very easily, so the small axons contain spins that have moved a large distance (via the ECS). In the very large axons, the spins in the center of the axons move freely since they do not encounter the boundary. However, in the middle range of the axons, the spins do not move freely inside the axons nor do many spins enter the axons from the ECS.

4.5 | Eigenvalues and eigenfunctions of the Laplace operator

In Figure 9, we show the Laplace eigenvalues whose length scales are larger than $L = 3 \mu\text{m}$ for Ω^{flat} . This corresponds to all the Laplace eigenvalues below the threshold determined by the length scale formula in Eq. (37). In the plot, the eigenvalues were normalized by the diffusivity, as they tend to scale linearly with a change of D . The eigenvalues increase at a linear pace, but for higher permeabilities, they increase faster, resulting in fewer eigenvalues below the threshold. For $L = 3 \mu\text{m}$, there are between 300 and 450 eigenvalues, depending on the permeability.

For all positive permeabilities, only the first eigenvalue is zero. However, for small permeabilities ($\kappa = 10^{-9} \text{ m/s}$, 10^{-5} m/s), there is a significant number of eigenvalues that are close to zero, before the eigenvalues then start to increase at a linear pace. This corresponds to an uncoupled regime, where there is one constant eigenfunction for each compartment (31 in total), and thus 31 zero eigenvalues. For higher permeabilities ($\kappa = 10^{-4} \text{ m/s}$, 10^{-3} m/s , 10^{-2} m/s , 1 m/s), this is no longer the case; the eigenvalues increase linearly from the beginning.

In Figure 10, we show seven selected non constant Laplace eigenfunctions on Ω^{flat} for two permeabilities. For $\kappa = 10^{-5} \text{ m/s}$, the eigenfunctions are clearly affected by the cell membranes, and each eigenfunction behaves like a linear combination of independent functions restricted to one axon at a time (or to the ECS), starting with a combination of nearly constant functions. This corresponds to the more uncoupled regime that was observed in Figure 9. For lower indices, the eigenfunctions are nearly constant in the axons, while for higher indices, the eigenfunctions become

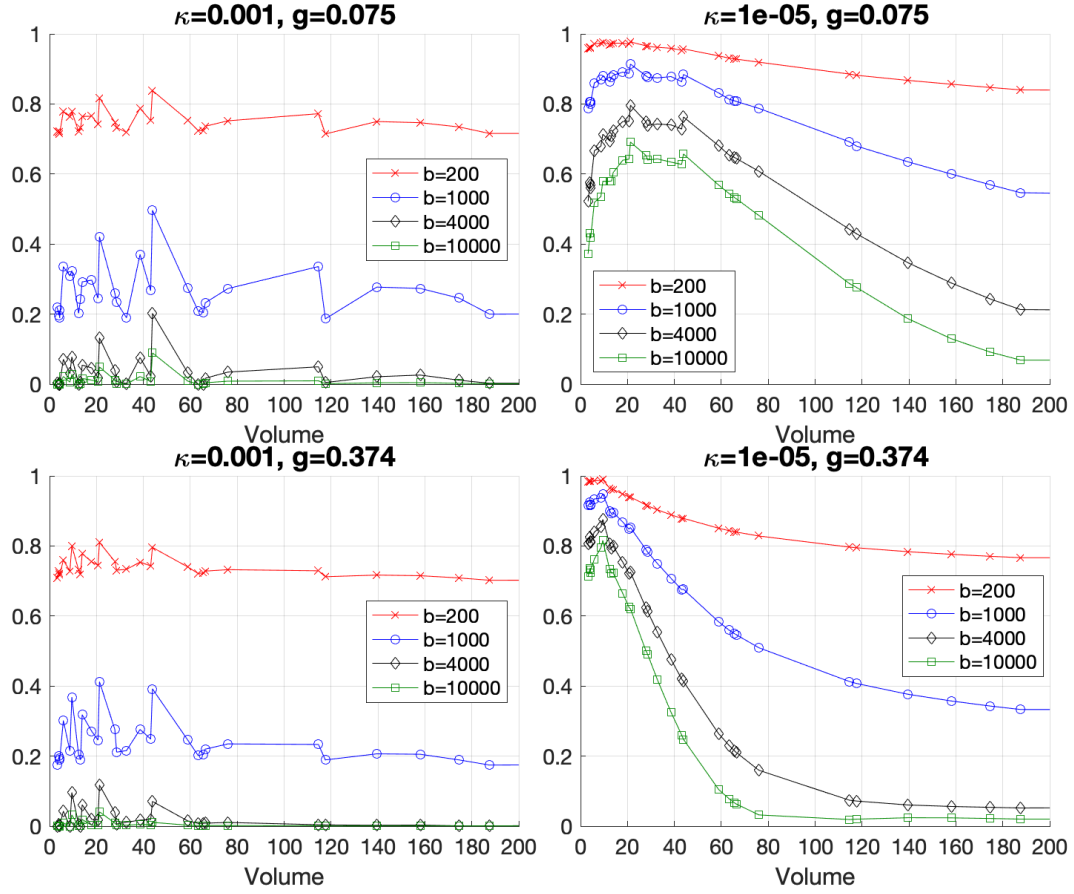


FIGURE 8 The 64 directions averaged compartment magnetizations \bar{M}_i on Ω^{flat} that were normalized by the compartment volumes (see Eq. (43)). The ECS compartment is not shown, as its volume is equal to $2119\mu\text{m}^3$, ten times more than the largest axon. The units are κ : m/s, $\|g\|$: T/m, b : s/mm², volume: μm^3 .

localized, either to one axon or to the entire ECS. For $\kappa = 10^{-4}\text{m/s}$, the functions are more connected, but still present jumps across the cell membranes. They also admit some localization for higher indices, but they are never entirely restricted to one compartment at a time. Interestingly, the eigenfunctions seem to coincide with the ones for $\kappa = 10^{-5}\text{m/s}$ for certain indices, for example 2, 150, or 410. But the high permeability eigenfunctions typically also include some features in the neighboring compartments, where the low permeability eigenfunctions are restricted to one compartment for the higher indices.

In Figure 11, we show twelve different Laplace eigenfunctions on Ω^{twist} for two permeabilities. For the higher permeability ($\kappa = 10^{-4}\text{m/s}$), the first functions have large length scales, and resemble directionalized sine waves with different orientations. For the lower length scale eigenfunctions, the oscillations are higher, but do in some cases admit an orientation in each of the axons, as can be seen for eigenfunction number 55 or 400. For the lower permeability ($\kappa = 10^{-5}\text{m/s}$), the different compartments act more separated, as was the case for Ω^{flat} . While the eigenfunctions in the ECS resemble those for the higher permeability, with diffusion being less restricted in the ECS, the eigenfunctions in the 30 axons seem to be nearly constant for the first 29 indices. For the higher indices, the eigenfunction support seem to be separated, where a function of one index only has non-zero values on some of the axons at the time. In the figure, the opacity of the insignificant axons was reduced to 15% to show the supports.

4.6 | Eigenvalues and eigenfunctions of the Bloch-Torrey operator

At high gradient amplitudes, it was demonstrated^{58,59} that in certain geometries (intervals, disks, spheres and the exterior of arrays of disks), the magnetization solution of the Bloch-Torrey equation exhibits localization near boundaries and interfaces. The analysis in those papers was based on the eigenfunctions of the complex-valued Bloch-Torrey operator,

$$-\nabla \cdot D\nabla + i\gamma g \cdot x,$$

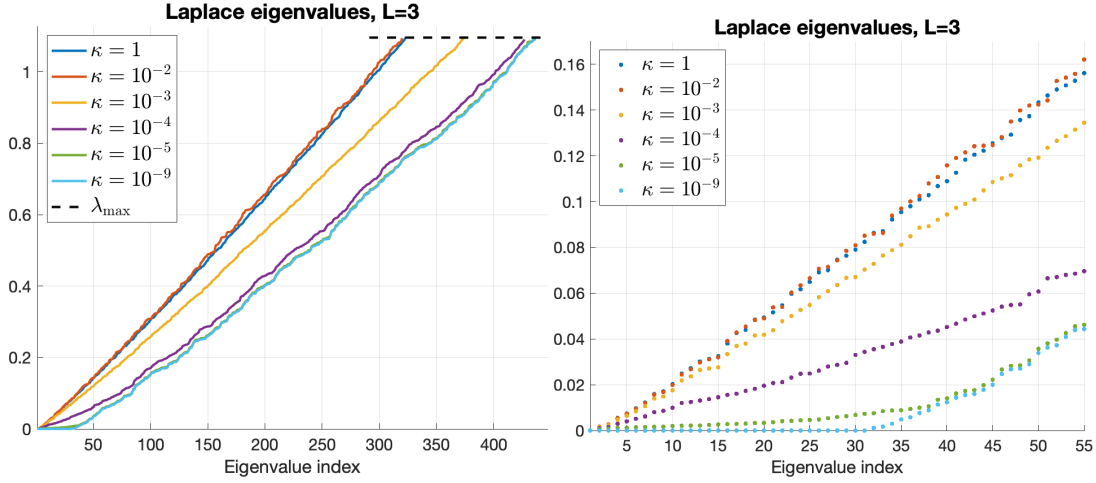


FIGURE 9 Laplace eigenvalues on Ω^{flat} , normalized by diffusivity (λ_n/D , given in μm^{-2}), for six permeabilities κ (m/s). Left: All eigenvalues with length scale above the minimum threshold $L = 3\mu\text{m}$. Right: zoom on the 50 most significant eigenvalues.

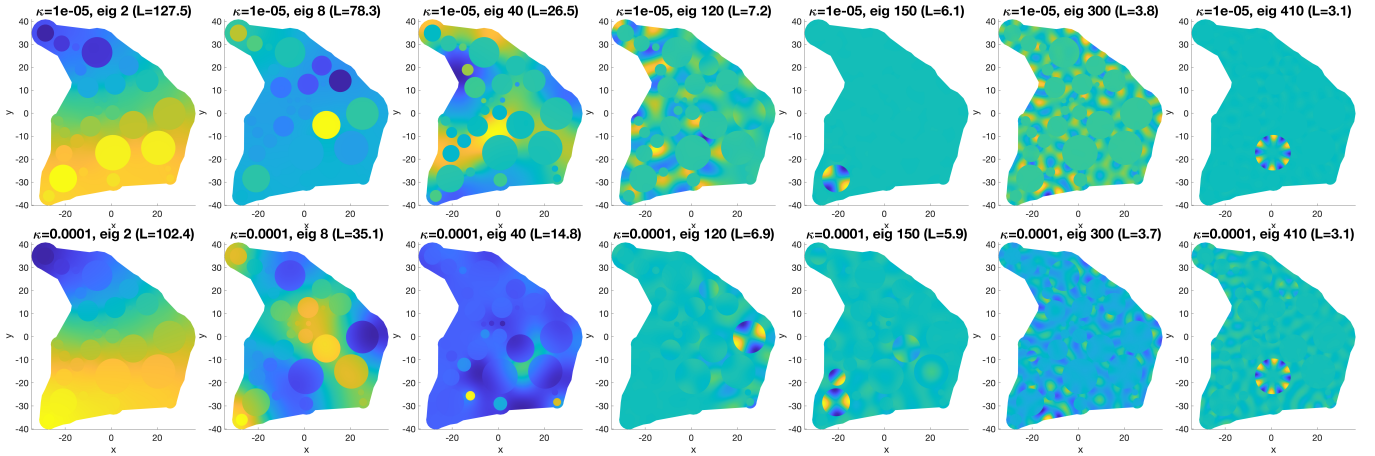


FIGURE 10 Seven selected non-constant Laplace eigenfunctions on Ω^{flat} with their associated length scales for two permeabilities κ . The colormap is unique to each plot, and is linear from blue to yellow. The actual values are not shown, but the eigenfunctions are orthogonal and normalized, with the first eigenfunction being constant. The units are κ : m/s, x, y, L : μm . The eigenfunctions are shown at the top layer ($z = 0.5\mu\text{m}$), but do not vary significantly in the z -direction for the length scales considered.

in contrast to the generalized Laplace operator $-\nabla \cdot D\nabla$. The conversion between the eigenfunctions of the Bloch-Torrey operator $(\psi_n)_{1 \leq n \leq N_{\text{eig}}}$ and the eigenfunctions of the Laplace operator $(\phi_n)_{1 \leq n \leq N_{\text{eig}}}$ is given by

$$\psi(\mathbf{x}) = \mathbf{V}^{-1} \phi(\mathbf{x}), \quad \psi = (\psi_1, \dots, \psi_{N_{\text{eig}}})^T, \quad \phi = (\phi_1, \dots, \phi_{N_{\text{eig}}})^T \quad (44)$$

where the columns of \mathbf{V} contain the eigenvectors of the complex-valued matrix $\mathbf{K}(g)$. The eigenvalues of the Bloch-Torrey operator are exactly the eigenvalues of $\mathbf{K}(g)$. We remind the reader that the eigenvalues of $\mathbf{K}(g)$,

$$\mu_1, \dots, \mu_{N_{\text{eig}}}, \quad 0 < \Re \mu_1 \leq \dots \leq \Re \mu_{N_{\text{eig}}},$$

are found on the diagonal of the matrix \mathbf{B} . We order the Bloch-Torrey (BT) eigenvalues and eigenfunctions by the magnitude of the real part of μ_i , all of which are strictly greater than 0.

In Figure 12, we show the complex eigenvalues of the 100 first (in order of increasing real part) BT eigenfunctions on Ω^{flat} and Ω^{twist} . We see that at the higher gradient amplitude, the BT eigenvalues have a wider range in their imaginary parts than at the smaller gradient amplitude. In terms of the magnetization, a larger range of the imaginary part indicates more time oscillations. For the higher permeability, the minimum real parts increase

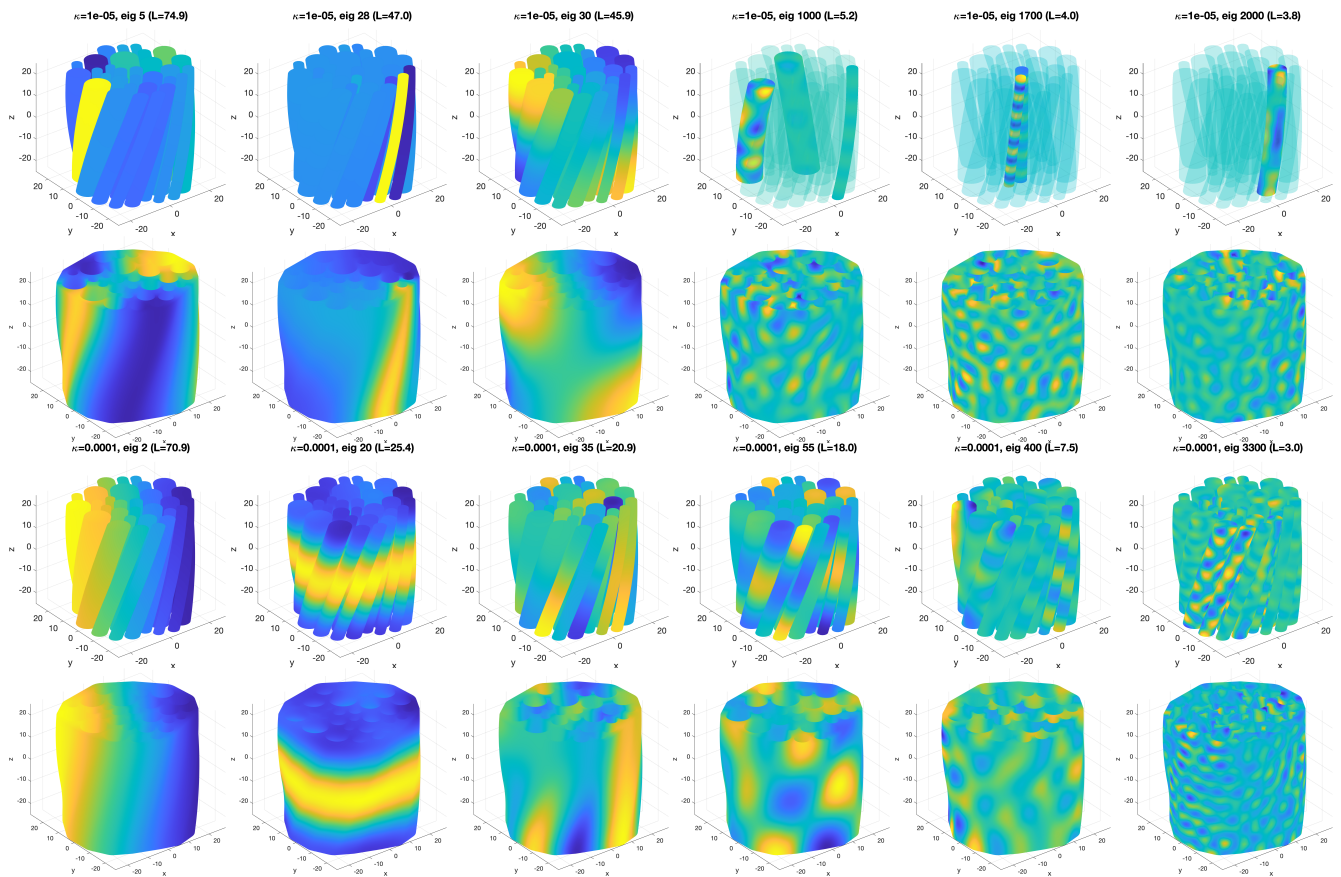


FIGURE 11 Twelve selected Laplace eigenfunctions of various length scales L on the geometry Ω^{twist} for two permeabilities $\kappa = 10^{-5}$ m/s (first two rows) and $\kappa = 10^{-4}$ m/s (last two rows). The 30 axons are shown in the first row for each permeability, and the ECS compartment in the second. The colormap is unique to each plot, and is linear from blue to yellow. The actual values are not shown, but the eigenfunctions are orthogonal and normalized, with the first eigenfunction being constant. In some of the plots, the axons where the eigenfunctions are close to zero compared to the most significant axons have a lower opacity (15%). The units are κ : m/s, x, y, z, L : μm .

with the gradient amplitude, which reflects a faster decay dynamic. For $\kappa = 10^{-5}$ m/s, the minimum real parts hardly increase with the gradient amplitude for Ω^{flat} because the diffusion in the gradient direction is hindered by the cell boundaries in the gradient direction. For Ω^{twist} however, the considered gradient direction has a vertical component. The vertical direction being rather unrestricted, as can be seen in the diffusion tensors in section 4.3 (despite the domain being twisted), the real parts of the eigenvalues do increase with the gradient amplitude. In order for signal attenuation to occur, the water molecules must be allowed to travel a certain distance without being hindered by cell membranes.

In Figure 13, we show some of the first Bloch-Torrey eigenfunctions on Ω^{flat} for two gradient directions, two gradient amplitudes and two permeabilities. For $\kappa = 10^{-5}$ m/s, each of the first 10 BT eigenfunctions is limited to one axon, and have nearly constant values on their respective supports. As the gradient direction changes, the BT eigenfunctions stay on the same supports, but their eigenvalues may change slightly, possibly leading to a reordering of the eigenvalues. For this reason, the BT eigenfunction index may change, as can be seen for BT eigenfunctions numbers 1 and 2 at $\|g\| = 0.075$ T/m. Eigenfunction 44 varies more, and is either limited to one axon or fills a larger and more diffuse zone in the ECS while still being localized. For $\kappa = 10^{-4}$ m/s, the eigenfunction supports extend beyond the cell membranes, and intersect with the supports of neighboring BT eigenfunctions. However, the first eigenfunctions still have most of their mass inside the axons. Higher index eigenfunctions, as eigenfunction 44, may be supported on the ECS.

In Figure 14, we show the magnitude of five complex-valued BT eigenfunctions on Ω^{twist} for two permeabilities. The same phenomenon as for Ω^{flat} is observed; the functions have clear, disjoint supports, limited to one axon at the time, and the higher permeability functions are slightly leaking into the ECS. However, unlike Ω^{flat} , the lower permeability eigenfunctions are never close to constant in their respective axons, but vary in the unrestricted direction.

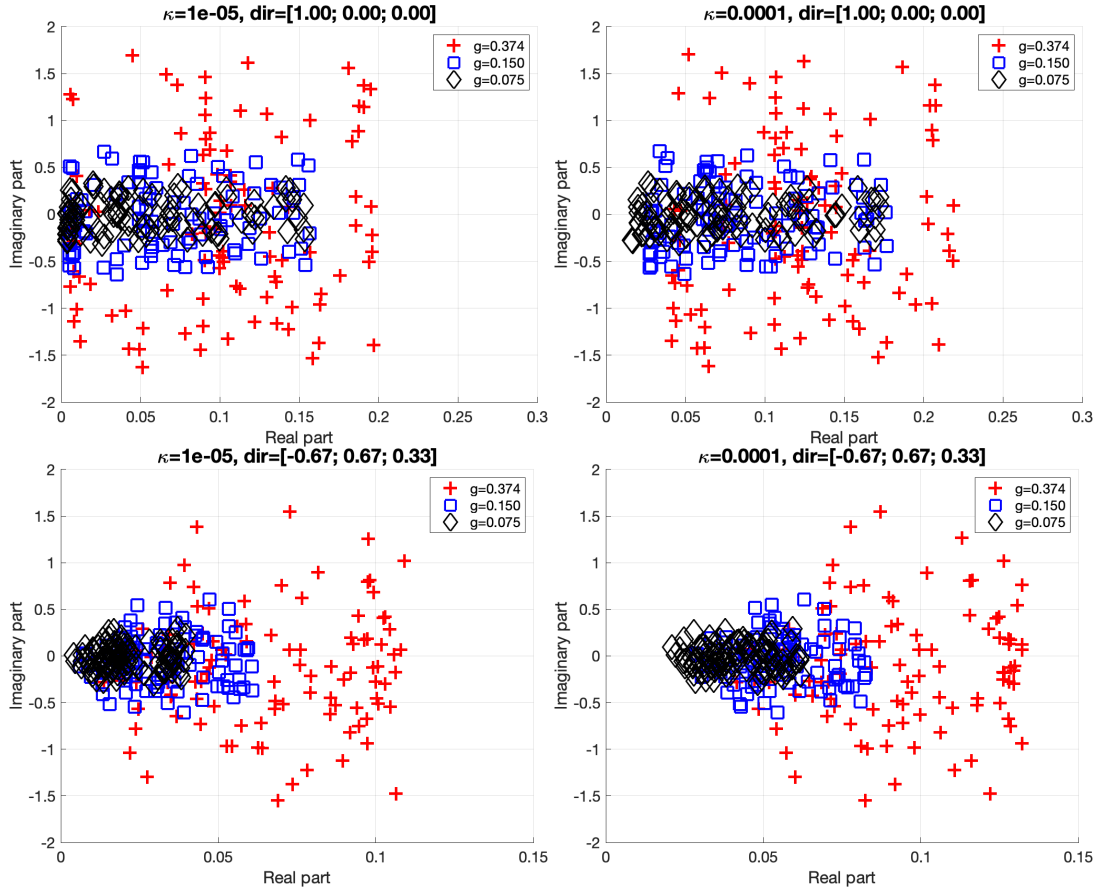


FIGURE 12 The 100 first complex Bloch-Torrey eigenvalues on Ω^{flat} (top row) and Ω^{twist} (bottom row) for two permeabilities. The eigenvalues are divided by the diffusivity (μ/D , given in μm^{-2}). For Ω^{flat} , the direction is $\mathbf{g}/\|\mathbf{g}\| = (1, 0, 0)^{\text{T}}$, and for Ω^{twist} , the gradient direction is $\mathbf{g}/\|\mathbf{g}\| = (-2/3, 2/3, 1/3)^{\text{T}}$. The units are $\kappa : \text{m/s}$, $\|\mathbf{g}\| : \text{T/m}$.

In order to examine how the BT eigenmodes affect the signal representation, the magnetization was computed on Ω^{flat} using a restricted number of BT eigenvalues in Eq. (24), while keeping all the Laplace eigenvalues (for a given minimum length scale L). The resulting relative errors with respect to the corresponding BTPDE-signals are shown in Figure 15. For shorter diffusion times, more components are needed to describe the signal, as less diffusion has occurred, and more of the details remain. More components are also needed for $\kappa = 10^{-5}\text{m/s}$ than for $\kappa = 10^{-3}\text{m/s}$, since the compartments are more isolated and the signal attenuates less. In most of the cases considered, an error of less than one percent can be attained by keeping the first 50-150 BT eigenfunctions. The remaining BT eigenmodes are redundant, and do not further decrease the error. Although the error decreases globally as the number of components increases, it is not guaranteed to decrease monotonically. This is because the BT eigenfunctions are not used to represent the solution during the entire gradient sequence, but only during the first part, and during the third part in a conjugate form. At $t = 0$, the initial spin density is first projected onto the Laplace eigenfunctions, before it is reprojected onto the BT eigenfunctions (multiplying the initial density with \mathbf{V}^{-1} in Eq. (24)). Each BT component is then attenuated and shifted exponentially according to the corresponding BT eigenvalue for a duration δ . The resulting magnetization is then expressed in the Laplace eigenfunction basis at time $t = \delta$ (multiplying the BT coefficient vector with \mathbf{V}), even in the case considered, where $\delta = \Delta$. These coefficients are reprojected onto the *conjugate* BT eigenfunction basis (multiplication with \mathbf{V}^*), before they are once again attenuated and shifted according to the conjugate complex eigenvalues (same attenuation, but inverse complex phase-shift). The conjugate BT coefficients are finally expressed in the Laplace basis (multiplying by \mathbf{V}^{-*}) at the final time step $t = T_e$. Because the matrix \mathbf{V} is not unitary (\mathbf{K} is not hermitian), the operation at $t = \delta$ (multiplying by $\mathbf{V}^* \mathbf{V}$) changes the BT coefficients. Using a larger subset of the BT indices in \mathbf{V} and \mathbf{V}^{-1} (keeping all the Laplace indices) is thus not directly linked to a decrease in the resulting error. It does however allow for the study of the contribution of each BT eigenmode.

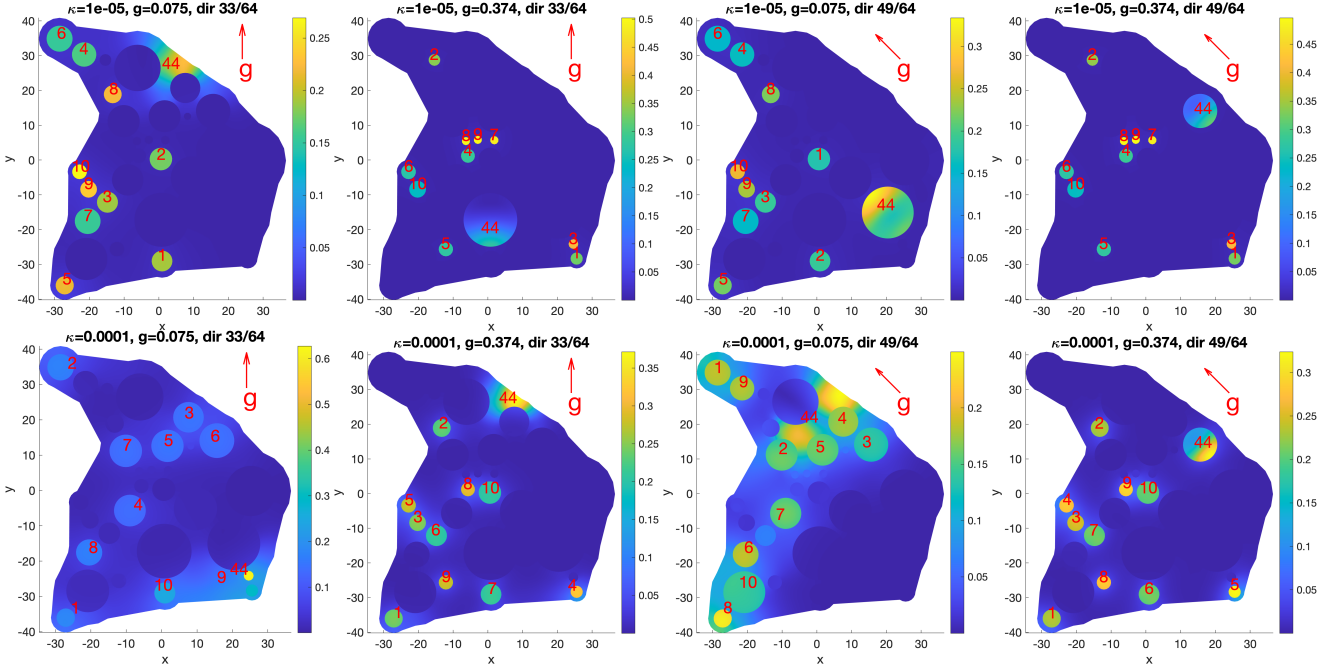


FIGURE 13 Magnitude of the first few complex-valued Bloch-Torrey eigenfunctions on Ω^{flat} for two values of κ (rows), two gradient directions (columns), and two gradient amplitudes (columns). The directions are $\mathbf{g}_{33}/\|\mathbf{g}_{33}\| = (0, 1, 0)^T$ and $\mathbf{g}_{49}/\|\mathbf{g}_{49}\| = (-\sqrt{2}/2, \sqrt{2}/2, 0)^T$. Because the BT eigenfunctions are “localized”, multiple eigenfunctions are plotted on the same domain (the magnitudes are summed up). The numbers correspond to the eigenfunction indices, and are placed in the center of mass of each eigenfunction support (where the magnitude is above 10% of its maximum value). At $\kappa = 10^{-5}$ m/s, there is no overlap in the supports of the plotted BT eigenfunctions. At $\kappa = 10^{-4}$ m/s, there is some overlap in the supports of the plotted BT eigenfunctions that are close to each other. The units are κ : m/s, $\|\mathbf{g}\|$: T/m, x, y : μm . Only the top layer of the eigenfunctions is shown ($z = 0.5\mu\text{m}$).

4.7 | Computational time

In Table 3 and 4 we give the computational times for Ω^{flat} and Ω^{twist} respectively. All the simulations were performed on a server computer with 12 processors (Intel (R) Xeon (R) E5-2667 @2.90 GHz), 192 GB of RAM, running CentOS 7, using MATLAB R2019a. It is clear that once the Laplace eigendecomposition has been computed, the Matrix Formalism signal representation can be obtained rapidly for many sequences, b-values, and gradient directions. We note that given N_{eig} eigenfunctions, the number of associated model parameters of the Matrix Formalism representation is $N_{\text{eig}} + 3N_{\text{eig}}(N_{\text{eig}} - 1)/2$, because the matrix \mathbf{L} is diagonal and the three matrices \mathbf{A}^x , \mathbf{A}^y , and \mathbf{A}^z are symmetric. The computational times are given for *one* gradient direction, while the Laplace eigendecomposition times are independent of the gradient direction. For Ω^{twist} , all the simulations were not performed at once, and the performance may depend on the traffic on the server computer at the time of computation. The MF timings for Ω^{twist} include the assembly of the nodal coordinates of magnetization field at $t = T_e$, given by $\mathbf{P}\mathbf{H}\nu$ – a dense matrix $\mathbf{P} \in \mathbb{R}^{N_{\text{node}} \times N_{\text{eig}}}$ multiplied by a dense vector $\mathbf{H}\nu \in \mathbb{C}^{N_{\text{eig}}}$. With $N_{\text{node}} = 146002$ and $N_{\text{eig}} \in \{2000, 3500\}$, this operation can be significant. For Ω^{flat} , the signal was computed directly with Eq. (22), reducing the computational time.

5 | DISCUSSION

We described a numerical implementation of the Matrix Formalism representation of the solution to the Bloch-Torrey PDE for permeable interior compartments and we have shown it to accurately represent the solution for a wide range of diffusion times and b-values. By using the Laplace eigenfunctions as a basis for the function space of solutions to the Bloch-Torrey PDE, the diffusion MRI signal can be computed for different gradient pulse sequences at low additional cost, once the Laplace eigendecomposition has been performed. By choosing to represent the Laplace eigenmodes using a length scale, the different eigenmodes can be linked to the physical length scales of the problem. Furthermore, this reduces

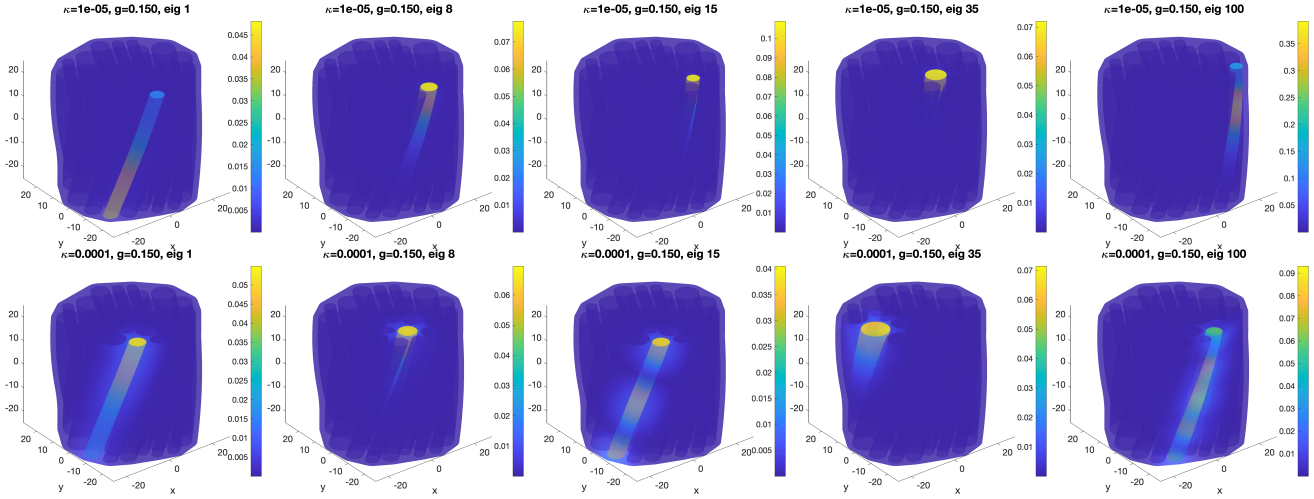


FIGURE 14 Magnitude of five complex-valued BT eigenfunctions on the geometry Ω^{twist} for two permeabilities $\kappa = 10^{-5}$ m/s (first row), $\kappa = 10^{-4}$ m/s (second row), one gradient amplitude $\|g\| = 0.150$ T/m, and one gradient direction $g/\|g\| = (-2/3, 2/3, 1/3)^T$. All compartments have an opacity of 60%. The units are κ : m/s, $\|g\|$: T/m, x, y, z : μm .

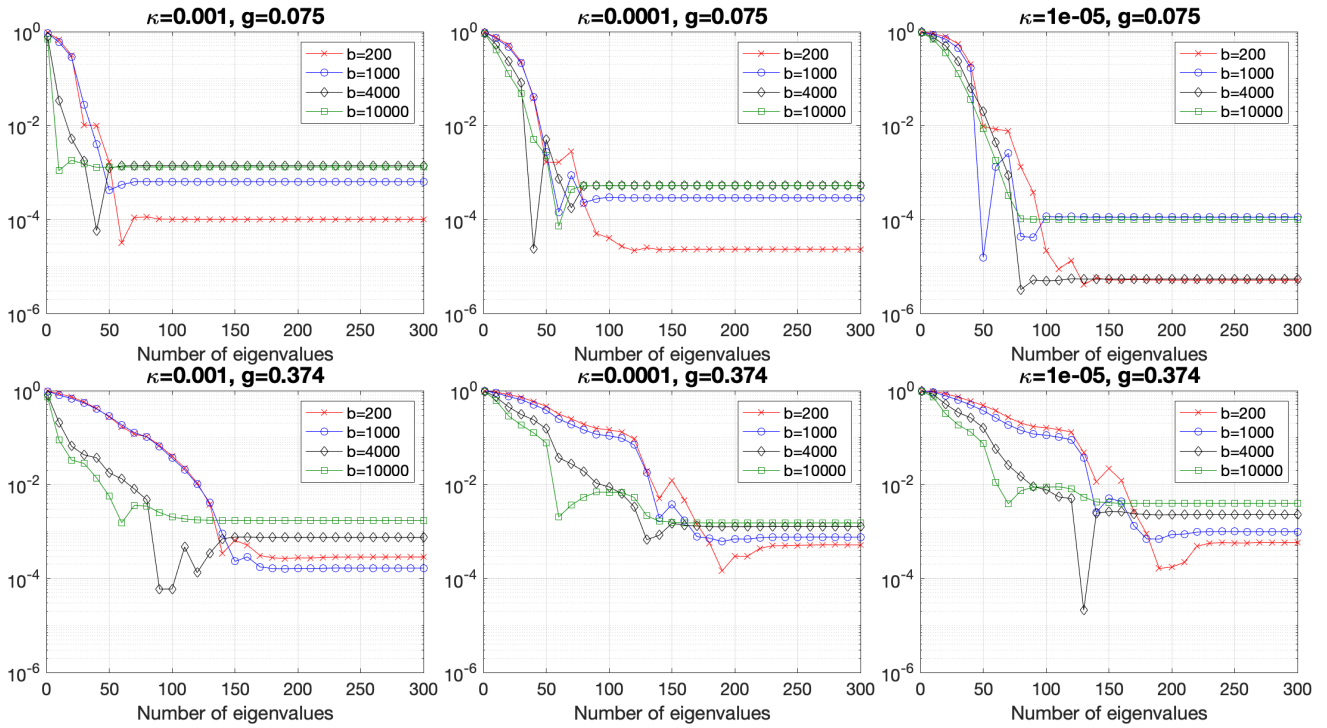


FIGURE 15 Relative difference $|S^{\text{MF}} - S^{\text{BTPDE}}|/|S^{\text{BTPDE}}|$ (not in percent) between MF and BTPDE direction averaged signals on Ω^{flat} , for different number of BT eigenvalues used. The minimum length scale is $L = 3\mu\text{m}$. The sequence is PGSE, $\delta = \Delta$. At equivalent b -value, a higher gradient amplitude indicates a shorter diffusion time. The units are κ : m/s, $\|g\|$: T/m, b : s/mm².

the computational time of the Matrix Formalism representation, as only a small subset of the Laplace eigenmodes are needed, as compared to the number of nodes in the finite element mesh.

The Matrix Formalism representation is not just of computational value, but also has analytical advantages. Replacing the finite element nodal basis $(\varphi_j)_{1 \leq j \leq N_{\text{node}}}$ by the Laplace eigenfunction basis $(\phi_n)_{1 \leq n \leq N_{\text{eig}}}$ and the BT eigenfunction basis $(\psi_n)_{1 \leq n \leq N_{\text{eig}}}$ is advantageous because the operators become diagonal and each mode can be studied independently of the others. The decay of the magnetization between the two gradient

κ	$\ \mathbf{g}\ $	δ	b	BTPDE (s)		MF (s)				
				H0.5	H0.2	H0.5 L3	H0.5 L2	H0.2 L3	H0.2 L2	
10^{-3}	Laplace eigendecomposition \rightarrow				103.218	213.267	249.202	510.955		
	0.075	5	33	8.636	18.548	0.073	0.392	0.085	0.503	
		10	267	11.316	23.461	0.075	0.422	0.092	0.548	
		20	2133	16.508	33.712	0.080	0.463	0.099	0.582	
	0.374	5	833	17.722	33.819	0.076	0.452	0.089	0.595	
		10	6666	32.628	62.361	0.080	0.483	0.099	0.628	
		20	53333	57.327	109.962	0.084	0.519	0.103	0.667	
	10^{-5}	Laplace eigendecomposition \rightarrow				134.275	226.226	275.265	568.945	
		0.075	5	33	8.702	18.172	0.097	0.490	0.105	0.605
10			267	11.329	23.208	0.098	0.522	0.103	0.636	
20			2133	19.702	40.506	0.108	0.586	0.113	0.677	
0.374		5	833	18.319	34.362	0.105	0.528	0.113	0.645	
		10	6666	36.317	70.450	0.113	0.570	0.117	0.669	
		20	53333	62.384	120.167	0.121	0.624	0.127	0.738	

TABLE 3 Computation times for the signal on Ω^{flat} for given diffusion-encoding sequences and gradient amplitudes, averaged over 64 directions. The units are κ : m/s, $\|\mathbf{g}\|$: T/m, δ : ms, b : s/mm², H : μm^3 and L : μm . All the computation times are in seconds. For MF, the Laplace eigendecomposition is only performed once for each permeability coefficient. For $\kappa = 10^{-3}$ m/s, there are 374 eigenvalues for $L = 3\mu\text{m}$ and 751 for $L = 2\mu\text{m}$. For $\kappa = 10^{-5}$ m/s, there are 436 eigenvalues for $L = 3\mu\text{m}$ and 821 eigenvalues for $L = 2\mu\text{m}$.

pulses of the PGSE sequence is controlled by the Laplace eigenvalues. During the two gradient pulses, the magnetization attenuates according to the real part of the BT eigenvalues and is phase-shifted according to the complex part. The BT eigenfunctions are more localized than the Laplace eigenfunctions, which can allow the analysis of the contribution of local regions to the diffusion MRI signal as possible future work. A possible way to build reduced models of the diffusion MRI signal in the brain white matter would be the inclusion of the most significant BT eigenfunctions for the type of cylinder geometries we simulated in this paper. The significant BT eigenfunctions would depend on the desired range of axon radii and on the range of diffusion times and b-values for which the reduced model is expected to be accurate. A library of BT eigenfunctions could be saved for many axon radii, and for the ECS associated with embedded axons of many radii distributions. This library can be used to build reduced models.

The positive permeability on the interior compartment boundaries resulted in new numerical challenges beyond the impermeable case that we addressed in our previous work. In this paper, we described how we overcame those challenges. In addition, we showed the effects of the interface permeability coefficient on the magnetization solution, on the Laplace eigenmodes, and on the Bloch-Torrey eigenmodes. The effects of the compartment boundaries become significant at lower permeabilities for both the Laplace eigenmodes and the BT eigenmodes. We have illustrated with numerical examples that the magnetization distribution is clearly affected by the exterior boundary as well as the boundaries of the interior compartments. At higher permeabilities, the diffusion is less restricted in the interior of the domain, and the outer boundary of the domain hinders the magnetization attenuation more than the interior cell boundaries. At lower permeabilities, the interior compartment boundaries hinder the diffusion strongly, with the smallest compartments impeding the magnetization attenuation the most.

Before our work, Matrix Formalism, as a closed form signal representation, though mathematically elegant, has not been used as a practical way of computing the diffusion MRI signal in complicated geometries. The calculation of the Laplace eigendecomposition in complicated geometries that include permeable interfaces using Monte-Carlo based simulations would be essentially impossible due to computational time and memory limitations. We have shown that, using the FEM, we were able to make the numerical computation of the Matrix Formalism achievable for such geometries. Our numerical implementation is available in an updated version of the SpinDoctor toolbox.

In this article, we considered compartments with constant diffusion coefficients and the piece-wise constant PGSE sequence. The Matrix Formalism representation can also be extended to consider compartment-wise constant diffusion tensors instead of diffusion coefficients, outer boundary relaxivity, T_2 -relaxation, and arbitrary magnetic gradient sequences, by using a piecewise constant approximation of the sequence³³. The new version of SpinDoctor has support for diffusion tensors, outer boundary relaxivity, T_2 -relaxation, and arbitrary diffusion-encoding sequences, including sin- and cos-type oscillating gradient spin echo (OGSE) sequences. Future work includes additional simulations using these extensions, including the non-uniform initial spin density formulation presented in the theory section, and a more systematic study of the contributions to the diffusion MRI signal from different geometrical length scales by analyzing the significant Laplace and BT eigenmodes at low interface permeability.

κ	δ	Δ	b	$\ g\ $	BTPDE (s)	MF (s)		
						$N_{\text{eig}} = 2000$	$N_{\text{eig}} = 3500$	
10^{-4}	Laplace eigendecomposition \rightarrow					29112	40339	
	5	5	1000	0.409	16838	37	197	
			3000	0.819	23082	40	211	
			7000	1.083	26893	43	218	
			10000	1.295	17214	43	218	
	10	50	1000	0.055	6747	34	173	
			3000	0.109	8667	36	188	
			7000	0.145	9704	37	187	
			10000	0.173	10492	37	192	
	10^{-5}	Laplace eigendecomposition \rightarrow					20676	39387
		5	5	1000	0.409	10028	38	188
				3000	0.819	13885	41	203
7000				1.083	15411	41	218	
10000				1.295	16602	44	218	
10		50	1000	0.055	6783	34	172	
			3000	0.109	8840	35	188	
			7000	0.145	9708	38	187	
			10000	0.173	10515	38	188	

TABLE 4 Average computation times per gradient direction for Ω^{twist} , given in seconds. The Laplace eigendecomposition is only performed once for each permeability coefficient, and is independent of the gradient direction. With $N_{\text{eig}} \in \{2000, 3500\}$, the minimum length scales are $L \in \{3.662\mu\text{m}, 2.901\mu\text{m}\}$ for $\kappa = 10^{-4}\text{m/s}$ and $L \in \{3.754\mu\text{m}, 2.954\mu\text{m}\}$ for $\kappa = 10^{-5}\text{m/s}$. The units are κ : m/s, δ, Δ : ms, b : s/mm², and $\|g\|$: T/m.

6 | CONCLUSION

We presented a numerical implementation of the Matrix Formalism representation for the diffusion MRI signal in domains that include *permeable* interfaces. The Matrix Formalism representation is based on Laplace eigenfunctions, which only need to be computed once per geometry, in contrast to the alternative method which directly solves the Bloch-Torrey PDE for each diffusion encoding gradient sequence. We described the computational techniques based on a finite element discretization and showed that our implementation to be accurate for a wide range of common simulation parameters. We also illustrated the effects of the magnitude of the permeability coefficient on the eigen-decompositions of the Laplace and the Bloch-Torrey operators. This numerical implementation is available in an updated version of the diffusion MRI simulation toolbox SpinDoctor.

DATA AVAILABILITY STATEMENT

The software and simulation setups are available in an updated version of the SpinDoctor toolbox. The source code can be found at <https://github.com/jingrebecali/SpinDoctor>.

ACKNOWLEDGMENT

The authors gratefully acknowledge the *Institut Carnot Télécom et Société Numérique* program and the *Centre de Mathématiques Appliquées at Ecole Polytechnique* for financially supporting the software engineer position of Syver Døving Agdestein.

References

1. Hahn E. L.. Spin Echoes. *Phys. Rev.* 1950;80:580–594.
2. Stejskal E. O., Tanner J. E.. Spin Diffusion Measurements: Spin Echoes in the Presence of a Time-Dependent Field Gradient. *The Journal of Chemical Physics*. 1965;42(1):288–292.
3. Bihan D Le, Breton E, Lallemand D, Grenier P, Cabanis E, Laval-Jeantet M. MR imaging of intravoxel incoherent motions: application to diffusion and perfusion in neurologic disorders.. *Radiology*. 1986;161(2):401-407. PMID: 3763909.
4. Palombo Marco, Ligneul Clémence, Najac Chloé, et al. New paradigm to assess brain cell morphology by diffusion-weighted MR spectroscopy in vivo. *Proceedings of the National Academy of Sciences*. 2016;113(24):6671–6676.
5. Abe Mitsunari, Fukuyama Hidenao, Mima Tatsuya. Water diffusion reveals networks that modulate multiregional morphological plasticity after repetitive brain stimulation. *Proceedings of the National Academy of Sciences*. 2014;111(12):4608–4613.
6. Reveley Colin, Seth Anil K., Pierpaoli Carlo, et al. Superficial white matter fiber systems impede detection of long-range cortical connections in diffusion MR tractography. *Proceedings of the National Academy of Sciences*. 2015;112(21):E2820–E2828.
7. Novikov Dmitry S., Jensen Jens H., Helpert Joseph A., Fieremans Els. Revealing mesoscopic structural universality with diffusion. *Proceedings of the National Academy of Sciences*. 2014;111(14):5088–5093.
8. Metcalfe-Smith E., Meeus E., Novak J., Dehghani H., Peet A., Zarinabad N.. Auto-regressive Discrete Acquisition Points Transformation for Diffusion Weighted MRI Data. *IEEE Transactions on Biomedical Engineering*. 2019;:1-1.
9. Dang S., Chaudhury S., Lall B., Roy P. K.. Tractography-Based Score for Learning Effective Connectivity From Multimodal Imaging Data Using Dynamic Bayesian Networks. *IEEE Transactions on Biomedical Engineering*. 2018;65(5):1057-1068.
10. Moutal N., Maximov I. I., Grebenkov D. S.. Probing surface-to-volume ratio of an anisotropic medium by diffusion NMR with general gradient encoding. *IEEE Transactions on Medical Imaging*. 2019;:1-1.
11. Christiaens D., Cordero-Grande L., Hutter J., et al. Learning Compact q -Space Representations for Multi-Shell Diffusion-Weighted MRI. *IEEE Transactions on Medical Imaging*. 2019;38(3):834-843.
12. Assaf Yaniv, Blumenfeld-Katzir Tamar, Yovel Yossi, Basser Peter J.. Axcaliber: A method for measuring axon diameter distribution from diffusion MRI. *Magn. Reson. Med.* 2008;59(6):1347–1354.
13. Alexander Daniel C., Hubbard Penny L., Hall Matt G., et al. Orientationally invariant indices of axon diameter and density from diffusion MRI. *NeuroImage*. 2010;52(4):1374–1389.
14. Zhang Hui, Hubbard Penny L., Parker Geoff J.M., Alexander Daniel C.. Axon diameter mapping in the presence of orientation dispersion with diffusion MRI. *NeuroImage*. 2011;56(3):1301–1315.
15. Zhang Hui, Schneider Torben, Wheeler-Kingshott Claudia A., Alexander Daniel C.. NODDI: Practical in vivo neurite orientation dispersion and density imaging of the human brain. *NeuroImage*. 2012;61(4):1000–1016.
16. Burcaw Lauren M., Fieremans Els, Novikov Dmitry S.. Mesoscopic structure of neuronal tracts from time-dependent diffusion. *NeuroImage*. 2015;114:18 - 37.
17. Palombo Marco, Ligneul Clemence, Valette Julien. Modeling diffusion of intracellular metabolites in the mouse brain up to very high diffusion-weighting: Diffusion in long fibers (almost) accounts for non-monoexponential attenuation. *Magnetic Resonance in Medicine*. 2017;77(1):343–350.
18. Palombo Marco, Ligneul Clémence, Najac Chloé, et al. New paradigm to assess brain cell morphology by diffusion-weighted MR spectroscopy in vivo. *Proceedings of the National Academy of Sciences*. 2016;113(24):6671–6676.
19. Ning Lipeng, Özarslan Evren, Westin Carl-Fredrik, Rathi Yogesh. Precise Inference and Characterization of Structural Organization (PICASO) of tissue from molecular diffusion. *NeuroImage*. 2017;146:452 - 473.

20. Fieremans Els, Jensen Jens H., Helpert Joseph A.. White matter characterization with diffusional kurtosis imaging. *NeuroImage*. 2011;58(1):177 - 188.
21. Panagiotaki Eleftheria, Schneider Torben, Siow Bernard, Hall Matt G., Lythgoe Mark F., Alexander Daniel C.. Compartment models of the diffusion MR signal in brain white matter: A taxonomy and comparison. *NeuroImage*. 2012;59(3):2241–2254.
22. Jespersen Sune N., Kroenke Christopher D., Astergaard Leif, Ackerman Joseph J.H., Yablonskiy Dmitriy A.. Modeling dendrite density from magnetic resonance diffusion measurements. *NeuroImage*. 2007;34(4):1473–1486.
23. Santis] Silvia [De, Jones Derek K., Roebroeck Alard. Including diffusion time dependence in the extra-axonal space improves in vivo estimates of axonal diameter and density in human white matter. *NeuroImage*. 2016;130:91 - 103.
24. Lee Hong-Hsi, Fieremans Els, Novikov Dmitry S.. What dominates the time dependence of diffusion transverse to axons: Intra- or extra-axonal water?. *NeuroImage*. 2018;182:500 - 510.
25. Novikov Dmitry S., Fieremans Els, Jespersen Sune N., Kiselev Valerij G.. Quantifying brain microstructure with diffusion MRI: Theory and parameter estimation. *NMR in Biomedicine*. 2019;32(4):e3998.
26. Novikov Dmitry S., Kiselev Valerij G., Jespersen Sune N.. On modeling. *Magnetic Resonance in Medicine*. 2018;79(6):3172–3193.
27. Fieremans Els, Lee Hong-Hsi. Physical and numerical phantoms for the validation of brain microstructural MRI: A cookbook. *NeuroImage*. 2018;182:39 - 61. Microstructural Imaging.
28. Renonnet Gaëtan, Scherrer Benoît, Girard Gabriel, et al. Towards microstructure fingerprinting: Estimation of tissue properties from a dictionary of Monte Carlo diffusion MRI simulations. *NeuroImage*. 2019;184:964–980.
29. Li Jing-Rebecca, Nguyen Van-Dang, Tran Try Nguyen, et al. SpinDoctor: A MATLAB toolbox for diffusion MRI simulation. *NeuroImage*. 2019;202:116120.
30. Fang Chengran, Nguyen Van-Dang, Wassermann Demian, Li Jing-Rebecca. Diffusion MRI simulation of realistic neurons with SpinDoctor and the Neuron Module. *NeuroImage*. 2020;222:117198.
31. Ascoli Giorgio A., Donohue Duncan E., Halavi Maryam. NeuroMorpho.Org: A Central Resource for Neuronal Morphologies. *Journal of Neuroscience*. 2007;27(35):9247–9251.
32. Callaghan Paul. A Simple Matrix Formalism for Spin Echo Analysis of Restricted Diffusion under Generalized Gradient Waveforms. *Journal of Magnetic Resonance*. 1997;129(1):74–84.
33. Barzykin Alexandre V. Theory of spin echo in restricted geometries under a step-wise gradient pulse sequence. *Journal of Magnetic Resonance*. 1999;139(2):342–353.
34. Grebenkov Denis. NMR survey of reflected Brownian motion. *Reviews of Modern Physics*. 2007;79(3):1077–1137.
35. Ozarslan Evren, Shemesh Noam, Basser Peter J.. A general framework to quantify the effect of restricted diffusion on the NMR signal with applications to double pulsed field gradient NMR experiments. *The Journal of chemical physics*. 2009;130(19292544):104702–104702.
36. Drobnjak Ivana, Zhang Hui, Hall Matt G., Alexander Daniel C.. The matrix formalism for generalised gradients with time-varying orientation in diffusion NMR. *Journal of Magnetic Resonance*. 2011;210(1):151–157.
37. Li Jing-Rebecca, Tran Try, Nguyen Van-Dang. Practical computation of the diffusion MRI signal of realistic neurons based on Laplace eigenfunctions. *NMR in Biomedicine*. 2020;33.
38. Grebenkov Denis S.. Pulsed-gradient spin-echo monitoring of restricted diffusion in multilayered structures. *Journal of Magnetic Resonance*. 2010;205(2):181–195.
39. Moutal Nicolas, Grebenkov Denis. Diffusion Across Semi-permeable Barriers: Spectral Properties, Efficient Computation, and Applications. *Journal of Scientific Computing*. 2019;81(3):1630–1654.
40. Lee Hong-Hsi, Fieremans Els, Novikov Dmitry S.. Realistic Microstructure Simulator (RMS): Monte Carlo simulations of diffusion in three-dimensional cell segmentations of microscopy images. *Journal of Neuroscience Methods*. 2021;350:109018.

41. Callaghan Paul T., Stepianik Janez. Frequency-Domain Analysis of Spin Motion Using Modulated-Gradient NMR. *Journal of Magnetic Resonance, Series A*. 1995;117(1):118-122.
42. Does Mark D., Parsons Edward C., Gore John C.. Oscillating gradient measurements of water diffusion in normal and globally ischemic rat brain. *Magn. Reson. Med.*. 2003;49(2):206-215.
43. Higham Nicholas J.. The Scaling and Squaring Method for the Matrix Exponential Revisited. *SIAM Journal on Matrix Analysis and Applications*. 2005;26(4):1179-1193.
44. Al-Mohy Awad, Higham Nicholas. A New Scaling and Squaring Algorithm for the Matrix Exponential. *SIAM Journal on Matrix Analysis and Applications*. 2009;31.
45. Al-Mohy Awad H., Higham Nicholas J.. Computing the Action of the Matrix Exponential, with an Application to Exponential Integrators. *SIAM Journal on Scientific Computing*. 2011;33(2):488-511.
46. Si Hang. TetGen, a Delaunay-Based Quality Tetrahedral Mesh Generator. *ACM Trans. Math. Softw.*. 2015;41(2):11:1-11:36.
47. Stewart G. W.. A Krylov-Schur Algorithm for Large Eigenproblems. *SIAM Journal on Matrix Analysis and Applications*. 2002;23(3):601-614.
48. Lehoucq R., Sorensen D., Yang C.. ARPACK users' guide - solution of large-scale eigenvalue problems with implicitly restarted Arnoldi methods. In: ; 1998.
49. Rahman Talal, Valdman Jan. Fast MATLAB assembly of FEM matrices in 2D and 3D: nodal elements. *Applied Mathematics and Computation*. 2013;219(13):7151-7158.
50. Ahrens James, Geveci Berk, Law Charles. *ParaView: An End-User Tool for Large Data Visualization*. Burlington, MA: Elsevier Butterworth-Heinemann; 2005.
51. Ayachit Utkarsh. *The ParaView guide : updated for ParaView version 4.3*. Clifton Park, New York: Kitware; 2015.
52. Shampine Lawrence F., Reichelt Mark W.. The MATLAB ODE Suite. *SIAM Journal on Scientific Computing*. 1997;18(1):1-22.
53. Grebenkov Denis S., Van Nguyen Dang, Li Jing-Rebecca. Exploring diffusion across permeable barriers at high gradients. I. Narrow pulse approximation. *Journal of Magnetic Resonance*. 2014;248:153-163.
54. Karger Jorg. NMR self-diffusion studies in heterogeneous systems. *Advances in Colloid and Interface Science*. 1985;23(0):129-148.
55. Fieremans Els, Novikov Dmitry S., Jensen Jens H., Helpert Joseph A.. Monte Carlo study of a two-compartment exchange model of diffusion. *NMR in Biomedicine*. 2010;23(7):711-724.
56. Li Jing-Rebecca, Nguyen Hang Tuan, Van Nguyen Dang, Haddar Housseem, Coatleven Julien, Le Bihan Denis. Numerical study of a macroscopic finite pulse model of the diffusion MRI signal. *Journal of Magnetic Resonance*. 2014;248(0):54-65.
57. Schiavi Simona, Haddar Housseem, Li Jing-Rebecca. A macroscopic model for the diffusion MRI signal accounting for time-dependent diffusivity. *SIAM Journal on Applied Mathematics*. 2016;. Accepted.
58. Grebenkov Denis S.. Exploring diffusion across permeable barriers at high gradients. II. Localization regime. *Journal of Magnetic Resonance*. 2014;248:164 - 176.
59. Moutal Nicolas, Demberg Kerstin, Grebenkov Denis S., Kuder Tristan Anselm. Localization regime in diffusion NMR: Theory and experiments. *Journal of Magnetic Resonance*. 2019;305:162 - 174.

